Electrochimica Acta 440 (2023) 141698

Contents lists available at ScienceDirect

Electrochimica Acta

journal homepage: www.journals.elsevier.com/electrochimica-acta

Quantifying transport and electrocatalytic reaction processes in a gastight rotating cylinder electrode reactor via integration of Computational Fluid Dynamics modeling and experiments

Derek Richard [a,1], Matthew Tom [a,1], Joonbaek Jang [a,1], Sungil Yun [a,1], Panagiotis D. Christofides [a,b,*,1], Carlos G. Morales-Guio [a,*,1]

[a] Department of Chemical and Biomolecular Engineering, University of California, Los Angeles, CA, 90095-1592, USA
[b] Department of Electrical and Computer Engineering, University of California, Los Angeles, CA 90095-1592, USA

ARTICLE INFO

Keywords:
Electrochemical reactor
CO_2 reduction
Digital twin
Electrocatalysis
CFD

ABSTRACT

Understanding the complexity of the multiple processes of mass, momentum, charge, and heat transport, and how these affect reaction kinetics at the electrode/electrolyte interface is one of the major challenges in the field of energy and catalysis. The rapid and rational scale-up of electrocatalytic systems to industrial scales require a detailed understanding of nonlinear transport-reaction processes, accessible only through the building of multi-physics models that capture with high fidelity the complexity of real-world devices. The gastight rotating cylinder electrode (RCE) reactor is a promising lab-scale tool that can decouple transport from intrinsic kinetics to generate data for first-principle models useful in the design of industrial, electrochemical reactors. Computational Fluid Dynamics (CFD) studies have previously been used to investigate the bulk flow in RCE reactors for simple corrosion and electroplating processes. However, the quantification of changes in local concentration within the viscous layer where catalysis takes place requires capturing the correct flow conditions inside the hydrodynamic boundary layer near the surface of the electrode. This requires simulations with spatial resolution in the nm and μm scale and temporal resolutions between ms and s scales that are similar to the timescales for reactions on the electrode surface. In this study, experimental electrocatalysis is combined with CFD modeling to elucidate and parameterize the hydrodynamics in a gastight RCE reactor. CFD simulations of the electrochemical ferricyanide reduction reaction under mass transport limited conditions are used to evaluate the validity of the CFD model parameters by comparing calculated dimensionless mass transport descriptors to dimensionless correlations obtained experimentally. Justifications for assumptions and details of the simulation methods used in this study are presented to provide a detailed understanding of the effect that each model parameter has on the ability to accurately simulate electrocatalysis in RCE systems. The simulation methodology reported here is a first step towards the development of multi-scale models for the study of transport dependent electrocatalytic processes, such as the electrochemical transformation of CO_2 to fuels and chemicals.

1. Introduction

Providing energy for a population projected to reach 9 billion people in the middle of this century is one of the most pressing societal issues. Today, fossil fuels comprising coal, oil, and natural gas products account for more than 80% of our global energy consumption [1]. Electrified chemical and fuel manufacturing systems promise to accelerate the renewable energy transition by replacing fossil-sourced molecules with molecules synthesized from air, water, and renewable electricity [2]. The efficient transformation of air and water into high-energy density molecules in an electrocatalytic reactor, however, requires precise control of the momentum, mass, charge, and heat transport phenomena as well as control of the reaction kinetics at the catalytic sites. Although substantial efforts have been made by the electrochemical engineering community [3] to develop a detailed understanding of the nonlinear transport-reaction relations in electrocatalytic reactors, a more detailed understanding of these processes is needed in order to rationally design and scale-up these technologies to commercially relevant scales.

* Corresponding authors at: Department of Chemical and Biomolecular Engineering, University of California, Los Angeles, CA, 90095-1592, USA.
E-mail addresses: pdc@seas.ucla.edu (P.D. Christofides), moralesguio@ucla.edu (C.G. Morales-Guio).
[1] All authors contributed equally to the research and writing of this article.

https://doi.org/10.1016/j.electacta.2022.141698
Received 16 October 2022; Received in revised form 8 December 2022; Accepted 9 December 2022
Available online 12 December 2022

In order to gain insight into complex electrocatalytic processes, we have recently developed a gastight rotating cylinder electrode (RCE) reactor for the study of electrocatalytic transformations under well-defined transport conditions. Fig. 1(a) shows schematically the different components of the RCE reactor, including the working and counter electrode compartments as well as the inlets and outlets for gases and the ports for sampling loops and auxiliary electrodes. The RCE reactor also includes a heating/cooling element to study the dependence of electrocatalytic transformations on temperature. Fig. 1(b) shows the RCE reactor under operating conditions as well as a digital image of the RCE shaft on which the active catalyst is mounted. The outlet of the gas in the headspace is connected to an online gas chromatogram and the back pressure on the cell is kept at atmospheric pressure unless indicated otherwise.

The RCE geometry has been chosen here as it offers a high degree of symmetry and homogeneity for primary and secondary current distributions on the surface of the electrode [3–5]. This allows the study of electrocatalytic processes under well-characterized electrochemical and hydrodynamic conditions. Although the rotating disk electrode (RDE) has been much more popular for the study of electrocatalysis under well-defined transport, few studies recognize that the primary current distribution in these electrodes is not uniform and that the concentration of species along the radial direction of the disk varies with position. In RDE systems, the potential drop in the solution, the concentration overpotential, and the surface overpotential vary with the radial position on the disk [6], and these gradients become larger for larger disks. This has limited the diameter of RDEs to 5 mm or less, and thus their use has also been limited for the fundamental study of electrocatalytic transformations that require accurate gas and liquid product quantification. Due to the limitations of the RDE system, Newman suggested that perhaps more attention should be devoted to the possibility of using rotating cylinder electrodes rather than rotating disk electrodes [3]. In our previous work, we have shown that the RCE cell is indeed a viable tool for the decoupling of intrinsic kinetics from transport effects and the extraction of high-quality data for the development of multi-physics electrocatalytic models, particularly for chemistries involving low solubility gases as reactants and low partial current densities for gas and liquid products [7]. A limitation of the RCE cell in Fig. 1(a) is, however, the fact that the counter electrode does not surround entirely the working electrode cylinder, which causes measurable distortions in the primary current distributions around the cylinder. These distortions become more significant under conditions of high current density and low electrolyte ionic conductivity.

The development of a multi-physics model of the RCE reactor will be of value for scale-up efforts if it reproduces with high-fidelity the experimental observations. Furthermore, by cross-validating the multi-physics model against a broad range of chemistries studied in the same cell and under the same hydrodynamic conditions, overparameterization will be reduced, and a deeper understanding of the relationship between transport and reaction processes at multiple time- and length-scales will be gained. Multi-physics models have the unique advantage of accessing multiple levels of spatial and temporal resolution, which cannot be achieved through experimental electrocatalytic or spectroscopic methods. From a fundamental heterogeneous electrocatalysis perspective, these models reveal time constants for processes that are obscured in experimental cells, such as the timescales for surface reaction and diffusion as well as the distribution of timescales for the transport of species in and out of the proximity of the electrode. From an engineering and scale-up perspective, a multi-physics model that is correctly parameterized could enable the accelerated *in silico* development of new electrocatalytic processes, where the complex and nonlinear interactions between transport and reactions are unknown to the experimentalist and yet, are captured in simulations carried out across multiple scales [8]. In this first work, we present a systematic approach and detail the initial process of parameterizing a multi-physics model of the gastight RCE reactor. Through the building of a multi-physics model for the RCE reactor, which has a rather simple and idealized geometry, we generate enough fundamental knowledge and know-how to explicitly list four minimum requirements needed in the development of high-fidelity multi-scale electrocatalytic models. These requirements are:

- The use of enhanced surface treatment functions at the electrode/electrolyte interface to capture accurately the momentum and energy transfer at the time- and length-scales relevant to electrocatalysis.
- The use of a fine mesh with a computational cell size at least one order of magnitude smaller than the characteristic length of the phenomena involved in the transport reaction process. For example, a computational cell size one order of magnitude smaller than the diffusion boundary layer thickness is needed to reveal the effects of cell hydrodynamics in the transport of species in and out of an electrocatalyst surface.
- The use of small simulation time steps to avoid numerical errors, but long simulated process times to capture transient behaviors that can then be validated against time-dependent experimental data.
- Validation of highly detailed simulations against correlations derived experimentally from high quality data that lump parameters relevant to the description of transport and reaction properties in the electrocatalytic cell. For example, the comparison of correlations between the dimensionless Reynolds (Re), Sherwood (Sh), and Schmidt (Sc) numbers obtained from simulations and experiments.

The multi-physics model presented in this work captures both the transport processes at the micrometer and microsecond scale occurring near the electrode/electrolyte interface, as well as the cell hydrodynamics and flow conditions developed in the system over millimeter and minute scales. The four minimum requirements listed here should inform further attempts to design, simulate, and construct electrocatalytic reactors at increasingly larger scales, and contribute to the accelerated scale-up of electrified chemical and fuel manufacturing systems by closing the existing gap between experimental electrocatalysis in bench-scale reactors and multi-scale models.

2. Experimental electrochemical methods in transport phenomena and catalysis

Among the various electrocatalytic transformations of relevance to the renewable energy transition, we have studied in the RCE reactor the electrochemical proton reduction to generate hydrogen (Eq. (1)), the electrochemical reduction of nitrites to ammonia (Eq. (2)), and the electrochemical reduction of CO_2 to fuels and chemicals such as liquid alcohols, ethylene, and carbon monoxide. The generation of carbon monoxide (Eq. (3)) is of particular interest as it is the first step in transforming CO_2 into all other further reduced hydrocarbons and alcohols. An additional reaction studied in the RCE reactor is the one-electron reduction of ferricyanide (Eq. (4)). This last reaction is used to characterize mass transport properties in electrochemical cells, as the kinetics on the surface of the electrode are fast, the entropy change in the process is small, and the reaction does not involve proton-coupled electron transfer steps that could be affected by changes in the local pH at the electrode/electrolyte interface.

$$2H^+ + 2e^- \rightleftharpoons H_2 \quad (1)$$

$$NO_2^- + 5H_2O + 6e^- \rightleftharpoons NH_3 + 7OH^- \quad (2)$$

$$CO_2 + H_2O + 2e^- \rightleftharpoons CO + 2OH^- \quad (3)$$

$$[Fe(CN)_6]^{3-} + e^- \rightleftharpoons [Fe(CN)_6]^{4-} \quad (4)$$

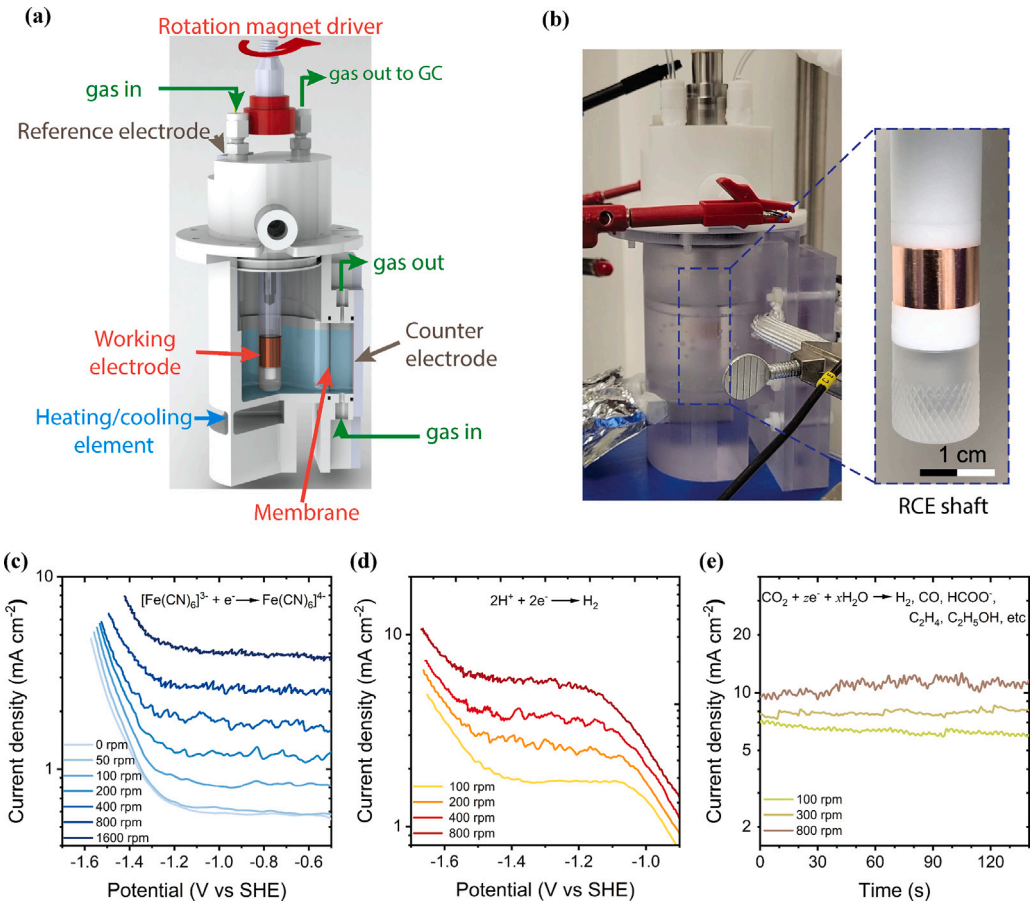

Fig. 1. (a) Schematic of the RCE reactor showing the separation between the working and counter electrode compartments. (b) Digital image of the RCE reactor under operation. The inset shows the insulating RCE shaft with an electropolished copper cylinder as the working electrode. (c) Current density vs. potential curves for the electrochemical reduction of ferricyanide on an electropolished copper cylinder electrode under different electrode rotation speeds. A 0.1 M potassium perchlorate solution with the addition of 0.01 M potassium ferricyanide was used as the electrolyte for ferricyanide reduction experiments at a scan rate of 50 mV s^{-1} at 20 °C. (d) Current density vs. potential curves for the electrochemical reduction of protons on a mechanically polished titanium cylinder electrode under different electrode rotation speeds at a scan rate of 50 mV s^{-1} at 20 °C. The electrolyte is a 0.05 M potassium perchlorate solution adjusted to a pH of 2.5 using perchloric acid. (e) Current vs. time curves for the electrochemical reduction of CO_2 on a nanoporous polycrystalline copper cylinder electrode in a 0.2 M $KHCO_3$ electrolyte at different rotation speeds. The applied potential is −1.28 V vs. SHE. Detailed experimental methods for electrode preparations are reported in [7].

$$2H_2O + 2e^- \rightleftharpoons H_2 + 2OH^- \quad (5)$$

Examples of experimental potential vs. current curves obtained for the reduction of ferricyanide and protons at 20 °C are shown in Fig. 1(c) and (d), respectively. At potentials positive of −1.4 V vs. the Standard Hydrogen Electrode (SHE), the current density for these two reactions is limited by mass transport, and increases as the rotation speed of the electrode increases. At potentials negative of −1.4 V vs. SHE, the competing hydrogen evolution reaction from water (Eq. (5)) takes place, resulting in a current density dependence on the applied potential, which is not observed for the reactions limited only by external mass transport at more positive potentials. Fig. 1(e) shows the current vs. time curves obtained during the electrochemical reduction of CO_2 to fuels and chemicals on a nanoporous polycrystalline copper electrode. In comparison to the ferricyanide and proton reduction in Fig. 1(c) and (d), the average current density for the electrochemical reduction of CO_2 shows a smaller dependence on the rotation speed when changing the rotation of the electrode from 100 to 800 rpm. In this case, the currents observed are the result of the complex coupling of transport and intrinsic surface reactions for multiple products, which cannot be readily separated.

Under mass transport limited conditions, the kinetics at the surface of the electrode are faster than the transport of reactants from the bulk of the electrolyte to the surface of the electrode. This large difference between intrinsic reaction and transport timescales results in transport-limited current densities j_{lim} independent of the applied potential. Under these conditions, the current densities are proportional to the bulk concentration of the reactant $C_{i,b}$, the number of electrons transferred per reacting molecule z, and the mass transport coefficient k_m (Eq. (6)). Here, the limiting current is i_{lim}, F is Faraday's constant, and the geometric area of the electrode is A.

$$j_{lim} = \frac{i_{lim}}{A} = zFk_mC_{i,b} \quad (6)$$

In the RCE reactor, we have experimentally measured the transport-limited current densities for the reactions in Eqs. (1) through (4) under different rotation speeds, reactant bulk concentrations, and temperatures. The details of these experiments have been previously discussed [7].

The transport-limited current densities provide a wealth of information on the transport phenomena occurring not only in the hydrodynamic boundary layer, but also within the first few electrolyte layers at the electrode/electrolyte interface through the small oscillations in the current density that occur as a function of time [9,10]. For example, the frequency and amplitude of the current oscillations are similar for the electrochemical reduction of ferricyanide and protons (Fig. 1(c) and (d)) indicating that these oscillations are related only to the transport phenomena and independent of the nature of the reactant molecules or the catalyst surface composition. As the rotation speed of the electrode increases from static conditions (with only gas bubbling in the bulk

of the cell) up to rotation speeds of 400 rpm, the amplitude and frequency of the current oscillations around an average value increase. When the rotation speed is higher than 400 rpm, the frequency of the current oscillations continues to increase while the amplitude of the current oscillations decreases. These changes in frequency and amplitude of the current density oscillations are the fingerprints of the different modes and timescales of mass, heat, and momentum transfer at the electrode/electrolyte interface and are important components in the process of describing how transport influences selectivity and conversion in electrocatalysis.

An accurate simulation of a complex and yet industrially relevant reaction such as CO_2 electrochemical reduction requires the correct parameterization of numerous interactions: such as heterogeneous reaction kinetics, homogeneous reaction kinetics, mass transfer between gas and liquid phases, as well as heat generation and transfer. This must also be done under non-ideal conditions with local changes in species concentration, and changes in applied surface potential when current distributions are not uniform. This requires a multiscale understanding of these interactions that is aided by the use of multiphysics models at multiple scales. This can be accomplished by separating a multi-scale, multi-physics model into three parts: (1) a CFD component that captures the continuum behavior of the reactor and transport phenomena at the macroscale (timescales of ms to minutes), (2) a molecular dynamics (MD) component that captures the interplay among the chemical events occurring at the mesoscale such as absorption and desorption processes at the electrode/electrolyte interface as well as buffer reaction kinetics and proton discharge events (μs to ms), and (3) an *ab initio* component that captures the energetics of making and breaking chemical bonds at the atomic scale for rare events that ultimately result in chemical or electrochemical step turnover (ns and ps). This work deals with the development of the CFD component.

The simulation of the CO_2 reduction process and other electrocatalytic transformations of similar complexity are beyond our current capabilities. The electrocatalytic reduction of protons and ferricyanide is a far simpler process than the electrocatalytic reduction of CO_2 to fuels and chemicals, and yet, it captures the same modes and timescales for transport phenomena occurring at the macroscale during the transformation of CO_2. For this reason, the ferricyanide reduction has been taken here as a starting point for the construction of complex multi-scale electrocatalytic models that can capture transport-reaction processes occurring in proximity to the electrode/electrolyte interface.

3. Emergence of universal transport-reaction correlations in RCE electrochemical cell

The rationale for the use of the simple ferricyanide reduction reaction as a starting point for the construction of the multi-physics model comes from the experimental observation of a universal correlation for transport and reaction processes in the RCE reactor, which is independent of the nature of the reacting molecule. We have experimentally observed that any molecule being reacted or generated on the surface of the rotating cylinder electrode will have to travel across the same fluid layers making up the turbulent flow conditions around the surface of the electrode [7]. From the transport-limited current densities shown in Fig. 1, mass transfer coefficients were calculated according to Eq. (6). Fig. 2(a) summarizes the experimentally measured mass transfer coefficients for solutions with high Sc above 100. High Sc indicates that the diffusion boundary layer (δ_d) will be small and shorter than the viscous sub-layer (δ_v). The mass transfer coefficients range from 0.0005 cm s^{-1} for the reduction of ferricyanide at electrode rotation speeds of 25 revolutions per minute (rpm), up to 0.01 cm s^{-1} for the reduction of protons at electrode rotation speeds of 800 rpm. Higher temperatures and higher rotation speeds result in higher mass transfer coefficients and thus, higher flux of reactants to the surface of the electrode.

Universal relations for different electrocatalytic transformations tested in the same electrochemical cell can be developed through the use of dimensionless numbers. In the RCE reactor, the experimentally obtained mass transfer coefficient can be transformed into its dimensionless mass transfer coefficient counterpart, Sh number, and can then be plotted against dimensionless descriptors of the hydrodynamics and intrinsic properties of the fluid, such as Re and Sc numbers. When this task is accomplished, a universal correlation emerges between the Sh, Sc, and Re numbers that is governed by the hydrodynamics of the fluid around the surface of the rotating cylinder electrode, and is independent of the nature of the molecules being transported in or out of the surface of the electrode. The experimental correlation for dimensionless mass transport and momentum transfer is shown in Fig. 2(b) for our RCE reactor. This correlation along with definitions for Re and Sc used in this study are also expressed in Eqs. (7), (8), and (9). Eq. (7) is of the same form as other experimental correlations that relate the limiting current densities to a power of the cylinder surface velocity.

$$Sh = \frac{k_{\mathrm{m}}}{D_i/d_{\mathrm{cyl}}} = 0.204\,Re^{0.59}Sc^{0.33} \tag{7}$$

$$Re = \frac{\rho U_{cyl} d_{cyl}}{\mu} \tag{8}$$

$$Sc = \frac{\mu}{\rho D_i} \tag{9}$$

Here the coefficient of 0.204 is a function of the cell geometry while the exponents on Re and Sc are a function of the hydrodynamics governing mass transfer to and from the electrode surface. ρ and μ are the bulk density and viscosity of the fluid, respectively, U_{cyl} and d_{cyl} are surface velocity and diameter of the rotating cylinder electrode, respectively, and D_i is the diffusivity of the reactant or product i. Similar correlations have been developed by Eisenberg et al. [11] and others Silverman [12], Selman and McClure [13] where an exponent of 0.50 to 0.70 for the Reynolds number has been suggested for smooth cylinders. Our experimental results indicate an exponent of 0.59. Differences in the exponent values are due to differences in convective transport across experimental cells of varying geometries, as discussed later in this work. The dependency of Sh as a power of near $2/3$ with respect to Re and $1/3$ with respect to Sc indicate that the penetration of eddies into the laminar sublayer play an important role in the mechanism of the mass transfer in the RCE for $Re > 500$ in the turbulent regime [14].

Fluid layers around the RCE are schematically shown in Fig. 3(a) and have been discussed in detail in the turbulent fluid dynamics literature. Mass transfer near the surface of the RCE is best understood through the description of the three distinct layers that form the hydrodynamic boundary layer (δ). Namely, the viscous sublayer δ_v, buffer layer, and turbulent logarithmic layer each with a uniquely predominant mode of mass transfer [15]. Near the surface of the electrode, the electrolyte in contact with the surface is in a non-slip condition and results in a quasi-static laminar sublayer or viscous sublayer where the predominant mode of mass transfer is diffusion. Beyond the viscous sublayer is the buffer or generation layer where both viscous shear stress generated at the electrode surface as well as the turbulent shear stress from the outer layer are too important to be ignored. Exceedingly energetic small-scale turbulence is generated here by the instability of the strongly sheared flow as a means to transform mean-flow kinetic energy to turbulent kinetic energy. Some of the turbulence generated here is carried outward into the broad outer layer of flow, and some is carried inward into the viscous sublayer. Finally, the fully turbulent logarithmic layer of the boundary layer is characterized by a mean fluid velocity that follows a logarithmic profile with the distance from the wall. Outside the boundary layer is the bulk flow region that contains most of the fluid and where convection is the predominant mode of mass transfer.

In our previous work in the electrocatalytic reduction of CO_2 on an electropolished polycrystalline copper cylinder electrode, we have

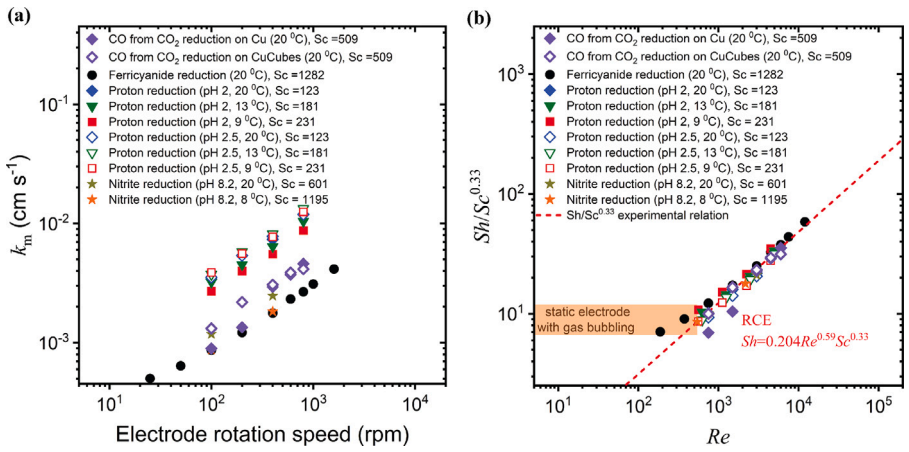

Fig. 2. (a) Experimental mass transfer coefficients determined under different electrode rotation speeds in the RCE cell. (b) Experimentally determined dimensionless relation between mass transfer and cell hydrodynamics for mass transfer coefficients in (a).

found that the residence time of CO near the surface of the electrode determines the degree of CO conversion to further reduced products such as methane, ethylene, ethanol, and propanol [7]. At a fixed surface applied potential, higher electrode rotation speeds, which correspond to higher Sh numbers, favor the production of the CO intermediate rather than the more reduced ethylene, methane, and alcohol products. The change in selectivity as a function of the Sherwood number was rationalized through the approximation of the electrode/electrolyte interface as a continuously-stirred tank reactor (CSTR; i.e., a control volume with inflow and outflow of reactants, intermediates, and products that is internally well-mixed) as schematically shown in Fig. 3(b). By creating a parallel between the different layers that build the turbulent boundary layer and the effects that we observe experimentally, we aimed to describe the rationale behind changes in selectivity as a function of the hydrodynamics in the cell. Faster electrode rotation speeds which result in higher Sherwood numbers result in increased rates of hydrogen and formate production, while the rate of CO_2 reduction to CO remains unchanged (Fig. 3(c)). Improved mass transport results in increased bicarbonate concentration and the lowering of the pH at the electrode surface, which should reduce proton concentration overpotentials relevant to the production of hydrogen and formate. On the other hand, the transformation of CO_2 to CO appears to be limited by CO_2 adsorption [16] and is not affected by changes in the concentration of protons which become more available at higher Sh numbers. In the case of CO_2 reduction, the rates of adsorption/electrosorption, as well as desorption are important and need more consideration. It becomes evident from the experimental data in Fig. 3(c) and (d) that the steady-state surface coverages of CO and hydrogen on the surface of the electrode are not enough to build micro-kinetic models for CO_2 reduction as these do not account for the residence time of intermediates in the proximity of the surface and the probability of collisions between surface-bound molecules and reactants traveling towards and away from the surface of the catalyst. That is, surface collision rates and the residence time distribution for reaction intermediates in the proximity of the electrode are determined by stochastic processes that can be only captured by molecular dynamic simulations and not by deterministic Fickian diffusion models frequently used in the simulation of CO_2 reduction processes.

The introduction of the concept of the residence time of reaction intermediates in multi-electron transformations is a complex idea to express in mathematical terms. There exists a residence time distribution for species in the proximity of the electrode and the average time that a reaction intermediate is available for further reaction, which will be a function of the diffusion, convection, and migration elements of the transport equations as well as the geometry of the cell. We have previously characterized the relative timescales for competitive transport and reaction processes utilizing experimentally determined Damköhler numbers. Damköhler numbers offer an experimental window into the relative timescales for these processes, but do not offer insight on the absolute timescales relevant to transport and reaction steps. Determining the absolute dimensions and timescales for reaction and transport components relevant to electrocatalysis is only possible through accurate multi-scale and multi-physics modeling.

However, before building complex multi-scale models, it is imperative to define a hierarchy of modeling techniques and to determine the relevant spatial and temporal resolutions at which each can provide insight (Fig. 3(b)). Typically, the computational cost of simulations increases as the physical scale of the interactions being modeled decreases, thus the timescales associated with these simulations are restricted. Efficient use of resources requires a top-down approach to be taken, where simulations of aggregate interactions occurring in the micrometer or greater scale (as with CFD) are performed first. This is particularly important for complex reactions such as the reduction of CO_2 where transport at the macroscale controls selectivity. Then, once these simulations are able to accurately capture the behavior of the system at the macroscale, more computationally expensive techniques such as MD or DFT, which investigate interactions on the nm and pm scale, can be integrated. Effectively integrating these modeling techniques together requires the delineation of the scales associated with the interactions being modeled, and coordination of the information that is passed between the models as boundary conditions at these scales. In such a manner, multi-scale modeling can be used for the development of accurate theories of electrocatalysis from first-principle quantum mechanics in regimes where reactions are not purely limited by mass transport and interactions are too complex to be evaluated by traditional techniques [17].

Numerous theoretical and computational works have been dedicated to the description of the transport processes in the rotating cylinder electrode reactor. CFD models developed so far, however, do not capture momentum and mass transfer between the solid and the liquid interface with the detail necessary to build high-fidelity multiphysics models of electrocatalytic transformations. That is, the determination of the concentration polarization and gradients in concentration emerging at the nanoscale near the surface of the electrode have not been calculated in multi-physics models.

4. Formulation of numerical simulation

Simulating fluid behavior is a balance between capturing pertinent details and optimizing the utilization of computational resources. Often times, due to computational resource limitations, relatively coarse meshes and universal velocity functions are used to reduce the computational resources required to run simulations in a reasonable time.

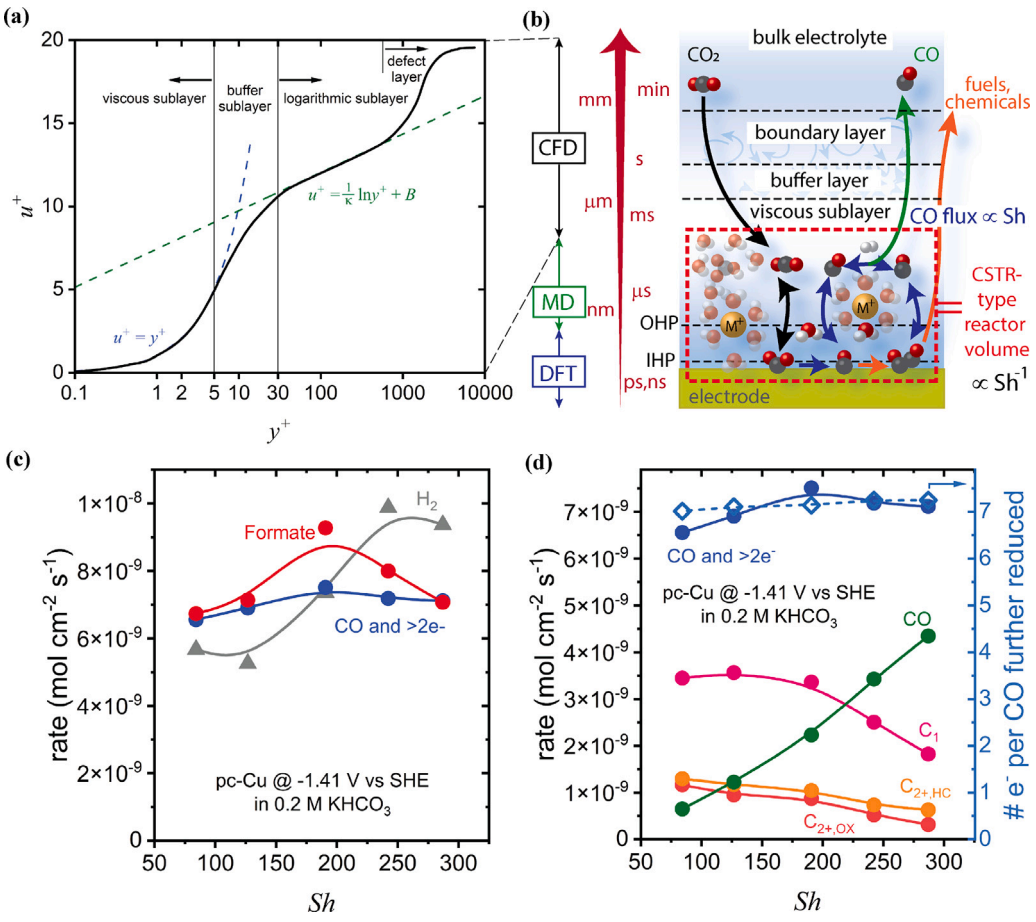

Fig. 3. (a) Normalized mean velocity profile in a turbulent boundary layer in semi-log coordinates. Illustrated are the various layers that make up the boundary layer. Here the Von Karman constant κ is 0.41 and B is 5 for turbulent flow over a smooth wall. (b) Schematic representation of a CSTR-type reactor volume at the electrode–electrolyte interface where CO production, desorption, re-absorption, diffusion, and further reduction take place. Transport and reactions steps occur at similar timescales within a narrow region inside the viscous sublayer. CO further reduction rates and product selectivity are affected by the mass transport within the cell as described by the Sh number. (c) Changes in the experimentally measured rates for CO_2 reduction in a 0.2 M $KHCO_3$ electrolyte at −1.41 V vs. SHE under different Sh number. (d) Changes in the conversion of the CO intermediate and the selectivity of further CO reduction products as function of the Sh number.

These simulations are typically performed using a steady-state solver method, and lack a comparison to transient data. While this approach may be suitable for evaluating the bulk behavior in a reactor, an investigation of the intrinsic fluid behavior and its impact on electrocatalysis requires a more detailed approach that can describe the transient behavior of the reactor, especially near the electrode surface. For example, Bauer et al. [18] simulated multi-ion transport in dilute electrolytic solutions around a rotating cylinder electrode and observed fluctuations in all physical fields (electric potential, concentration, and flow fields) occurring near the electrode surfaces. Fluctuation in all physical fields also result in temporal and spatial fluctuations in the boundary mass fluxes and thus, the local current densities and the total measured currents. The fluctuations in current densities and their relation to local mass transfer rates were first described by Van Shaw and Hanratty [19] for turbulent flow in a pipe wall and then by Matić et al. [20] for ferricyanide reduction on a rotating cylinder electrode. It is well understood that the small eddies in the region of the viscous sublayer of a turbulent flow, play an important role in determining the transfer rates to the wall, especially in the case of high Sc. Since the flow of these small eddies is unsteady, the local mass transfer rates to the wall are fluctuating [14]. A complete discussion of early methods utilized for the study of diffusion-controlled electrochemical reactions and their applications in the study of transport phenomena was reported by Mizushina [9] and Selman and Tobias [10]. For a model to truly capture the fluid behavior in an RCE, it is necessary to capture the mechanisms causing the fluctuations in current density, as observed experimentally in Fig. 1. To do this, careful consideration must be made in developing a method capable of resolving the fluid behavior extensively to the surface of the electrode.

The following sections will discuss the details of our final simulation methods, where multiple iterations of mesh and solution methods were tested to determine an accurate approach for simulating the hydrodynamics of the RCE. Understanding why the methods described here were chosen is just as important as understanding why other methods were not. Thus, alongside a detailed explanation of the methods, specific examples are provided to explain why these methods were selected.

4.1. Geometry simplification

Experimental data (Fig. 3(c) and (d)) and boundary layer theory (Fig. 3(a)) suggest that the most important hydrodynamic effects in the RCE occur near the electrode surface for mass transport affected reactions. This location is where the diffusion boundary layer is formed that governs the rate at which species can move to and from the catalytic surface inside the viscous sub-layer. In the bulk, turbulent mixing that occurs even at relatively low rpm should ensure a well-mixed solution, and at a first approximation, can be assumed to have little effect on transport at the electrode surface. With this in mind, the geometry of the reactor was simplified to reduce computational cost while maintaining the features necessary to accurately model the reactor behavior.

The geometry of the working electrode compartment in the RCE reactor is not entirely cylindrical, as it has an expanded section in the direction of the counter electrode to accommodate the ionic membrane and counter electrode compartment (Fig. 4(a)). The height and diameter of the fluid phase was maintained in the simulation geometry and was modeled into a symmetric cylindrical geometry shown in Fig. 4(b). The reference electrode and gas sparger are tubes of 4 and 3 mm diameter, respectively, located in the bulk region of the fluid (Fig. 4(a)). Because these tubes are located near the outer wall (more than 1.5 cm from the rotating cylinder surface), they are considered to have a minor role in determining the transport properties relevant to electrocatalysis at the rotation speeds of interest and were removed in the simplified geometry as illustrated in Fig. 4(b). All dimensions of the rotating cylinder electrode shaft were maintained consistent with the actual RCE reactor. This includes a cylinder diameter of 1.2 cm, an electrode length of 0.8 cm, and location of the electrode and shaft consistent with the RCE reactor. All relevant dimensions are provided in Fig. 4(b). Simulations at rotation speeds between 100 and 800 rpm were performed with this simplified geometry. To verify that the features removed for the simplified geometry do not have a significant impact on the hydrodynamics relevant to electrocatalysis in the RCE, a simulation geometry exactly matching that of the real RCE reactor, including all the features removed in the simplified geometry, was also tested. This reactor accurate geometry was extracted from the CAD file used in the construction of the actual gastight RCE reactor. This accurate geometry was also tested with gas bubbling to verify the insignificance of bubbling on the reaction conditions in the accurate geometry. For simplicity the simplified reactor geometry used for the bulk of the simulations in this study will be referred to as the *simplified geometry* while the geometry used to verify the performance of the simplified geometry will be referred to as the *accurate geometry*.

4.2. Mesh generation

A non-uniform mesh with polyhedral mesh type was used in the majority of the geometry volume. Polyhedral mesh creates cells with more faces than other mesh types, and because of this connection with a large number of adjacent cells, is best suited to simulate swirling or mixing flows like those created in turbulent mixing found in the RCE. Finer mesh was used in regions near boundaries and interfaces while coarser mesh was used in regions where gradients in velocity and concentration are expected to be minimal as shown in Fig. 4(c). A structured mesh was used to help capture the boundary layer region near the shaft surface where fluid motion is expected to be primarily in the azimuthal direction. This boundary layer mesh was made of 20 layers with a growth rate of 1.25 and an initial cell height of 3 μm, resulting in a total thickness of 1029 μm. A closeup of the boundary layer mesh with dimensions is provided in Fig. 4(d). These dimensions were chosen after testing other configurations to enable good resolution of the diffusion boundary layer and viscous sublayer to enable accurate simulation of both momentum and mass transfer at the shaft surface.

The final mesh resulted in a total of 859,897 cells. Quality measures including the orthogonal quality and squish were both within acceptable ranges, with a minimum orthogonal quality of 0.15 and a maximum squish of 0.85 [21]. Average values for orthogonal quality and squish show much better quality for the majority of the cell, with an orthogonal quality having an average of 0.98, and squish having an average value of 0.023. All lower quality cells reside at the surface near the corner created at the bottom of the shaft due to the sharp curvatures of the geometry. Since these cells have little impact on the overall hydrodynamics, these values were considered adequate. Additionally, the aspect ratio has a maximum value of 357 and an average value of 21. While the maximum value is outside of the specifications by ANSYS [21], these cells with high aspect ratio are all located in the boundary layer mesh where fluid flow is known to be almost entirely parallel to the shaft. Because of this, the high aspect ratio in this region should not affect the results of the simulation and allows for a reduction in the cell count and time to run simulations. Overall, the mesh quality of the multi-physics model is classified as *excellent*, the highest level based on specifications outlined in the ANSYS Manual, which ensures the convergence of simulations and the accuracy of the numerical solutions [21].

4.3. Fluid flow

All simulations were performed with ANSYS Fluent simulation software using a finite volume method. A pressure-based, solution method was used along with the multiphase, volume of fluids, and full multicomponent diffusion models. Incompressible fluids under turbulent flow are described by the Reynolds averaged Navier–Stokes (RANS) equation (Eq. (10)) and the continuity equation (Eq. (11)).

$$\rho\left(\frac{du}{dt}+u\cdot\nabla u\right)=-\nabla P+\nabla\cdot(\mu+\mu_{\mathrm{T}})\left(\nabla u+(\nabla u)^{T}\right) \tag{10}$$

$$\nabla\cdot(\rho u)=0 \tag{11}$$

Here, u is the averaged velocity vector in cylindrical coordinates with components u_θ, u_r, and u_z in the respective azimuthal, radial, and axial directions. ρ is the density, P is the pressure, μ is the fluid viscosity, and μ_{T} is the turbulent viscosity. The realizable $\kappa-\epsilon$ turbulence model was used to describe the turbulent fluid region where the turbulent viscosity μ_{T} is provided by Eq. (12).

$$\mu_{\mathrm{T}}=\rho C_{\mu}\frac{\kappa^{2}}{\epsilon} \tag{12}$$

in this equation κ is the turbulent kinetic energy, ϵ is the turbulent energy dissipation rate, and C_μ is a turbulence model variable calculated from realizable $\kappa-\epsilon$ theory. Both RANS [22] and realizable $\kappa-\epsilon$ theory [23] have been discussed in detail elsewhere.

To resolve the fluid behavior near the rotating surface, an enhanced surface treatment method was used. This method employs the turbulent viscosity described by Eq. (12) in the turbulent logarithmic region and the one equation model of Wolfshtein [24] in the viscous sublayer where μ_T is defined by Eq. (13).

$$\mu_{\mathrm{T,lam}}=\rho C_{\mu}l_{\mu}\sqrt{\kappa} \tag{13}$$

l_μ is a length scale factor calculated using Eq. (14) [25].

$$l_{\mu}=yC_{l}^{*}\left(1-e^{-Re_{y}/A_{\mu}}\right) \tag{14}$$

where y is the normal distance from the wall, Re_y is the turbulent Reynolds number, A_μ is a constant equal to 70, and $C_l^*=\kappa C_\mu^{-3/4}$ with $\kappa=0.41$. Turbulent viscosities in this two-layer approach are blended using Eq. (15) [26].

$$\mu_{\mathrm{T,enhanced}}=\lambda_{\epsilon}\mu_{T}+\left(1-\lambda_{\epsilon}\right)\mu_{\mathrm{T,lam}} \tag{15}$$

Here λ_ϵ is a blending function that is dependent on Re_y.

For the momentum balance, the dimensionless velocity is defined separately for the laminar (Eq. (16)) and turbulent (Eq. (17)) region near the wall [27,28]

$$u_{lam}^{+}=y^{+}\left(1+\frac{\alpha}{2}y^{+}\right) \tag{16}$$

$$\frac{du_{turb}^{+}}{dy^{+}}=\frac{1}{\kappa y^{+}}\left[S'\left(1-\beta u^{+}-\gamma\left(u^{+}\right)^{2}\right)\right]^{1/2} \tag{17}$$

where,

$$S'=\begin{Bmatrix}1+\alpha y^{+} & for\ y^{+}<y_{s}^{+}\\ 1+\alpha y_{s}^{+} & for\ y^{+}\geq y_{s}^{+}\end{Bmatrix} \tag{18}$$

Here, the superscript $^+$ indicates a nondimensionalization by the shear velocity $u_\tau=\sqrt{\tau_w/\rho_w}$, the viscous length scale $\delta_\nu=\mu_w/\left(u_\tau\rho_w\right)$, and ρ_w, where τ_w, ρ_w, and μ_w are the shear stress, density, and dynamic viscosity evaluated on the wall, respectively. For instance, $u^+=u/u_\tau$,

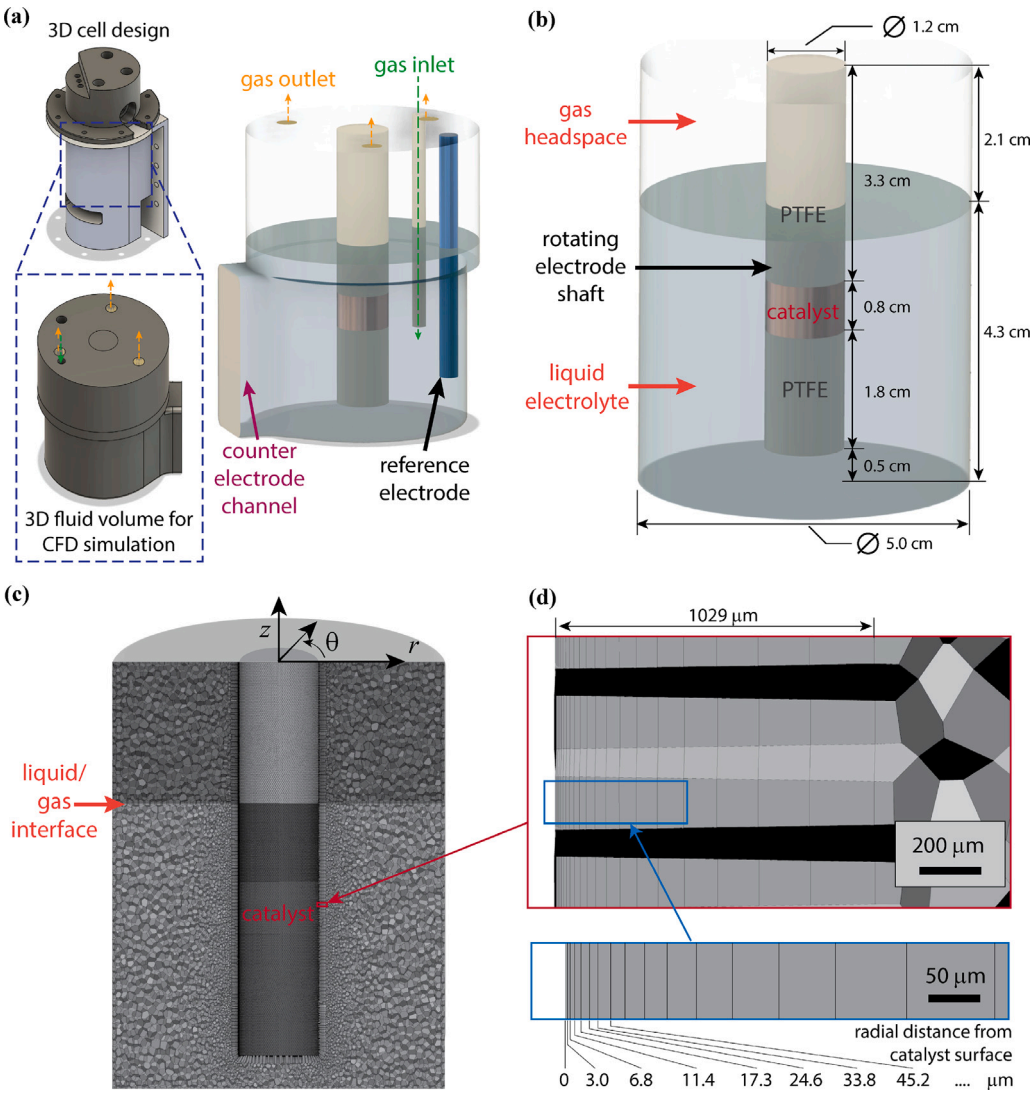

Fig. 4. 3D geometries used for CFD simulations. (a) Accurate geometry extracted from gastight RCE Computer Aided Design (CAD) files. (b) Simplified geometry used for simulations. The simplified geometry in (b) does not include the counter electrode channel, reference electrode, gas inlet tube, and bubbling of gas through the inlet which are present in the experimental RCE reactor. Simulation data was primarily collected using the simplified geometry in (b) which results in saving computation time. The accurate geometry in (a) was used to verify that the assumptions made for the simplified geometry do not affect the electrocatalysis simulation results. (c) Cross section of the final polyhedral volumetric mesh used in this study for the simplified geometry. Cylindrical coordinates used in the description of the reactor are shown for reference with components u_θ, u_r, and u_z in the respective azimuthal, radial, and axial directions. (d) Closeup of the structured boundary layer mesh at the surface of the shaft with the corresponding radial positions relative to the electrode.

$y^+ = y/\delta_v$, etc. Additionally, α, β, and γ are coefficients that account for the influence of pressure and thermal effects. y_s^+ is the location at which the log-law slope is fixed. By default, $y_s^+ = 60$.

To achieve continuity between the two layers, laminar and turbulent velocities are blended [29] according to Eqs. (19) and (20).

$$u^+ = e^{\Gamma} u_{lam}^+ + e^{\frac{1}{\Gamma}} u_{turb}^+ \tag{19}$$

$$\Gamma = -\frac{a\left(y^+\right)^4}{1+by^+} \tag{20}$$

where $a = 0.01$ and $b = 5$. A similar approach is also applied for thermal transfer at the wall. In this way, the simulation is able to utilize a fine mesh near the wall region that is capable of resolving the diffusion boundary layer, while still allowing a coarser mesh to be used in the bulk flow region (Fig. 4(c)). Initial simulations ran with the standard wall function approach did not perform well when compared with experimental data and theory. This led us to adopt the enhanced surface treatment which was found to adequately capture the behavior of the experimental cell from both a theoretical and experimental standpoint. A more detailed explanation for this approach will be discussed below.

For boundary conditions, a non-slip boundary condition was defined at all walls. Since the reactions of interest occur under mass transport limited conditions and the use of a supporting electrolyte renders migration effects negligible, electrochemical effects can be ignored. Instead, the reaction at the electrode surface was defined as shown in Eq. (21) without a dependence on applied potential.

$$\text{rate} = k_0 \cdot C_{i,s} \tag{21}$$

Here, the reaction rate coefficient k_0 was selected to be large enough that the ferricyanide concentration at the electrode surface approaches zero for all rotations speeds. This approach allows for the condition of a mass transport limited reaction to be simulated without the complexity of electrochemical interactions. The electrode shaft was set to have an angular velocity ω in rad s^{-1} defined for each rotation speed according to Eq. (22).

$$\omega = \frac{2\pi f}{60} \tag{22}$$

where f is in revolutions per minute (rpm). All other surfaces were defined as walls without flux or motion. In the simulation, properties for ferricyanide and ferrocyanide were taken to be the same as water due to the dilute nature of the solution. Diffusivity for ferricyanide and ferrocyanide in water were defined as 6.3×10^{-6} cm^2 s^{-1} and 5.6×10^{-6} cm^2 s^{-1}, respectively [30].

Due to the unsteady nature of turbulent flow, a transient solution method was used for all simulations where each simulation started with stagnant fluid and the hydrodynamics were allowed to evolve over time to reach a pseudo-steady-state flow condition before activating the reaction conditions on the surface of the electrode. The reader should be certain to distinguish the steady-state conditions discussed here from the steady-state solver used in other publications. The steady-state solver provides a single, *average* snapshot of the flow conditions in the reactor at steady-state, whereas our simulation uses a transient solver to resolve the fluid flow over time. Steady-state for the purposes of this publication refers to the condition where the change in average velocity of the fluid in the simulation fluctuates steadily around a single value. In this manner, we can still visualize the local fluctuations in velocity as a function of time throughout the reactor, but also know that the simulation has reached conditions where the momentum generation and annihilation are equal and there is no change in the average velocity field with time. Ensuring this condition before initiating the reaction at the catalyst surface was important for comparison with experimental data where the flow conditions in the reactor have been given time to reach steady state before inducing an electrochemical reaction.

Simulation time steps used for each rotation speed were tuned to ensure accurate and stable simulation with a Courant number less than one by reducing the time step until further reduction no longer yielded changes in the simulation results. As such, finite time step sizes of 2, 1, 0.5, 0.4, 0.25, and 0.2 ms were used for rotation speeds of 100, 200, 300, 400, 600, and 800 rpm respectively. All simulations were performed on the Hoffman2 Shared Cluster provided by UCLA Institute for Digital Research and Education's Research Technology Group using a 36-core dual processor with 192 GB of RAM. Due to the *steady-state* flow requirement of these simulations, we found that each simulation took about one week to reach a simulated time when this condition was met. While the scaling of the time step size with rotation speed reduced the computer processing time per second of simulated time, the amount of simulated time that was required to reach steady-state flow was longer for simulations with larger step sizes. The increase in simulation time required for low rotation speed was simply due to slower transfer of momentum from the shaft into the bulk of solution caused by the smaller velocity gradient. This resulted in similar computer processing time for all rotation speeds of 7 to 10 days to reach simulated times when steady-state flow conditions were reached. After integrating reaction chemistries in ANSYS Fluent, simulations were run for another 7 to 10 days to reach at least 20 s of process time. All simulations required a unique time for the reaction rate to develop mass transfer limited conditions, so steady-state reaction conditions were defined to be after 10 s of simulated time with reactions enabled. Estimates of the time required for the diffusion boundary layer to develop, were highest for 100 rpm at approximately 5 s. Thus, allowing 10 s of simulated time for equilibration was considered adequate, and a minimum of 10 additional seconds to observe the steady-state behavior was used in evaluating reaction conditions at steady state.

4.4. Evaluation of simulation method

The previous sections describe our final simulation method for capturing the hydrodynamics of the RCE reactor. However, the justification for this method is best evaluated in comparison to other methods we tested that did not yield accurate results. As such, this section provides greater detail about the impact of each key method used on the local conditions in the simulation, as well as the overall impact on the simulation performance.

We found that the key aspects necessary to accurately simulate the RCE reactor were the use of the enhanced surface treatment method combined with an adequately refined mesh that together provide good resolution of the concentration and hydrodynamic boundary layer. Initial simulations were performed similarly to previously reported RCE CFD simulations where a universal velocity function was assumed at the wall of the rotating cylinder using a standard wall function. However, this wall treatment method is designed for a coarse mesh where the diffusion boundary layer is not resolved. Because of this simplification, using a mesh that is sized to resolve the boundary layer causes issues when determining the velocity profile at the wall. Fig. 5(a) shows this issue, where a sharp drop close to the wall is observed when the standard wall function is used with our initial mesh, which is problematic for accurately predicting momentum transport at the shaft surface. In comparison, the enhanced wall treatment method, using the two-layer approach, is designed to be used with a fine mesh near the wall that can resolve each layer of the hydrodynamic boundary layer. Since a fine mesh is required to capture the diffusion boundary layer, the enhanced surface treatment method is well-suited to capture momentum transfer at the wall. As illustrated in Fig. 5(a), the enhanced surface treatment method is better able to capture the hydrodynamic boundary layer by providing a smooth transition in velocity as a function of the distance from the wall. This profile is closely matched to what would be expected based on turbulent boundary layer flow theory. In addition to the enhanced surface treatment methods, an adequately fine mesh is required at the wall to capture both momentum transfer and the physics of the diffusion boundary layer. This can be demonstrated by comparing the results obtained for a boundary layer mesh composed of ten 37-μm thick cells, to our final boundary layer mesh that is 20 layers thick and has a first cell height of 3 μm. While a slight increase in momentum transfer from the wall can be discerned in Fig. 5(a) when the mesh is refined, the effect is more significant for the diffusion boundary layer. Fig. 5(b) shows that while changing to an enhanced surface treatment method helps capture the curvature of the diffusion boundary layer better than the standard wall function, the coarse mesh is simply not fine enough to capture the concentration gradient at the wall. This results in only five cells inside the boundary layer and a near linear approximation for the changes in concentration as a function of position. However, when the refined mesh is used, the full curvature of the diffusion boundary layer is captured (shown in red) by ten cells at 800 rpm. This refinement also improved the ability of the simulation to capture the momentum transfer from the surface to the fluid, allowing the simulation to resolve the viscous sublayer and capture vortex formations near the surface that was obscured by the coarse mesh.

Besides the local differences displayed in Fig. 5(a) and (b), the impact of these methods on overall performance of the simulation in describing the reaction rate or current density can be observed in Fig. 5(c). Here, the standard wall function (shown in black) does not capture fluctuations in the current density. Non-fluctuating current density is to be expected with the $\kappa-\epsilon$ turbulence model and the standard wall function because this model is an averaging approach that does not capture the individual random fluctuations of turbulent flow. However, the magnitude of the current density is lower than expected. By implementing the enhanced surface treatment method, fluctuations can be observed in the current density (shown in gray). While the $\kappa-\epsilon$ model still does not allow resolution of the random turbulent fluctuations in the velocity field, the two-layer approach employed by the enhanced surface treatment method does allow structured vortices (non-random) inside the hydrodynamic boundary layer to be captured. Further discussion and justification for these surface vortices are provided in the discussion of the simulation results. Further refinement of the mesh to fully resolve the diffusion boundary layer and utilization of the enhanced surface treatment method, together, provided both the disturbances to the current density and the correct magnitude of current density (shown in red). This result is due to the increased resolution of mass transport in the diffusion boundary layer.

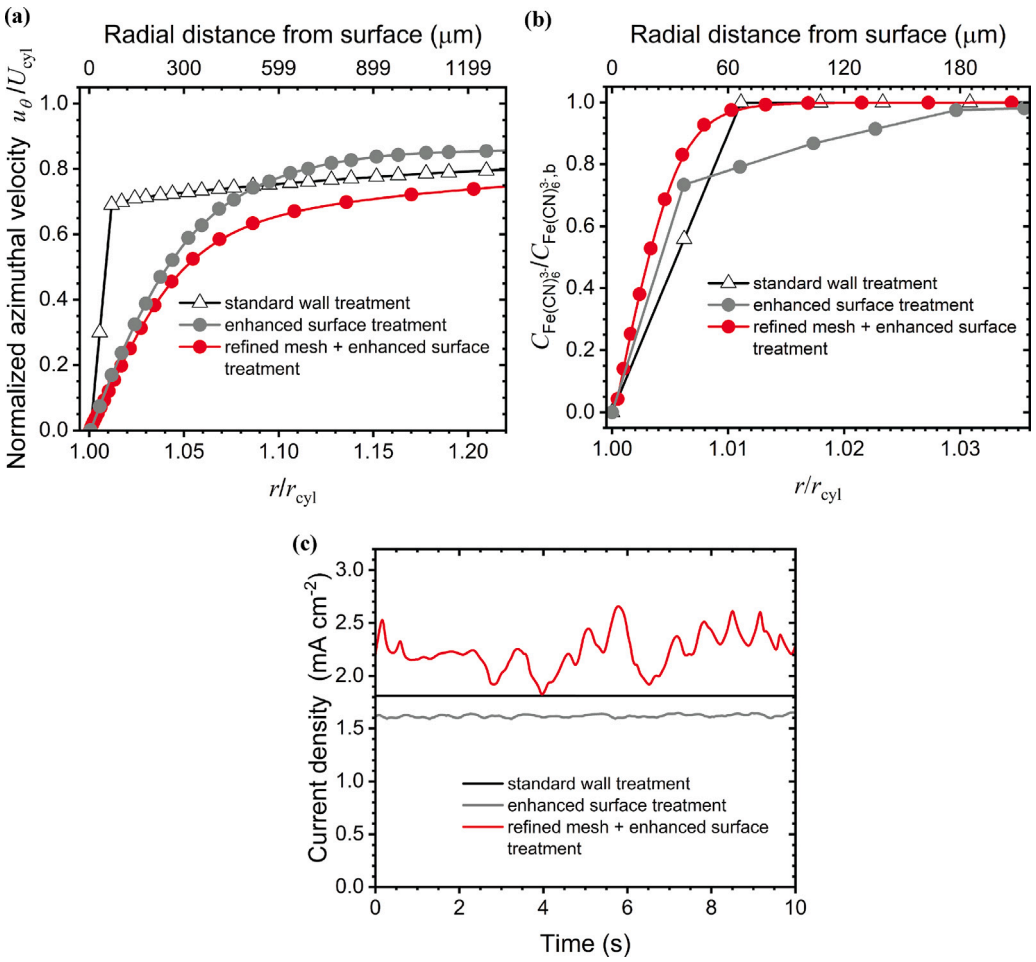

Fig. 5. CFD simulation results for the electrochemical reduction of ferricyanide in the RCE reactor at a rotation speed of 800 rpm. Effect of surface treatment method and mesh refinement on simulation of the (a) hydrodynamic boundary layer, (b) diffusion boundary layer, and (c) transient current density.

5. Results and discussion

Accuracy of the simulation in modeling the performance of the experimental RCE reactor can be evaluated by at least two metrics: agreement with the previously discussed universal dimensionless relationship for mass transport and closely matched transient behavior of the current density. While the dimensionless relationship helps evaluate the ability of the simulation to capture the time averaged multiscale nature of the reactor as *Re* is increased, the transient behavior of the current density informs us of the ability of the simulation to capture the mechanisms of mass, heat, and momentum transfer at the electrode surface. As mentioned previously, small oscillations in the current density as a function of time are commonly observed in experimental electrocatalysis. These ossilations have been attributed to eddy or vortex formations [25] on the electrode surface due to the turbulent conditions that are created even at particularly low rotation speeds for rotating electrodes or by the bubbling of gases in cells using static electrodes. The fluctuations in the current density observed experimentally are thought to be a unique fingerprint of the reactor hydrodynamics. Modeling this behavior is necessary to gain insight as to how the hydrodynamics of the RCE affect its performance.

Beginning with the universal dimensionless relationship between *Sh* and *Re* shown in Fig. 6(a), we observe that there is excellent agreement between the simulated results and experimental data. High rpm results align closely with the experimentally derived relationship for our gastight RCE reactor. The correlation derived by Eisenberg, Tobias, and Wilke for ferricyanide reduction in an RCE reactor on a flat rotating cylinder electrode is also plotted to show the agreement between the results of our RCE and previously published correlations for similar reactor geometries [11,31]. Slight differences in correlation constants are common for different reactor and electrode geometries, but all correlations fall close to the same line [4,32]. At low rpm, the simulation also captures the deviation from the correlation that we observe experimentally for ferricyanide reduction shown by the black dots. The agreement between the experimental and simulated transient current density can also be discerned in Fig. 6(b). Not only is the magnitude of the current density well-matched, but also the frequency and amplitude of the fluctuations. Most notable is how the frequency and amplitude change with rotation speed in both the experimental and simulation results. Together, agreement with the universal relationship and transient behavior, suggest that the simulation method presented here, accurately captures the hydrodynamics of the RCE reactor. To confirm that the assumptions made in simplifying the reactor geometry used in these simulations were justified, a comparison is made to simulations ran using the accurate geometry at 400 rpm. These simulations were performed using meshing and solution methods identical to that of the simplified mesh shown in Fig. 4(c) to ensure a direct comparison. The major assumption used in the geometry simplification was that disturbances in the bulk of the reactor have a minor effect on the hydrodynamics in the near wall region that is relevant to electrochemical reactions. Indeed, we find that bulk disturbances have minimal effect on mass transport to the surface of the catalyst. These disturbances can be identified in Fig. 6(a) by the close alignment of the data points collected using the simplified and accurate geometries. Even when gas bubbling was introduced, the difference between the simplified and accurate geometry results were minimal. This observation is not

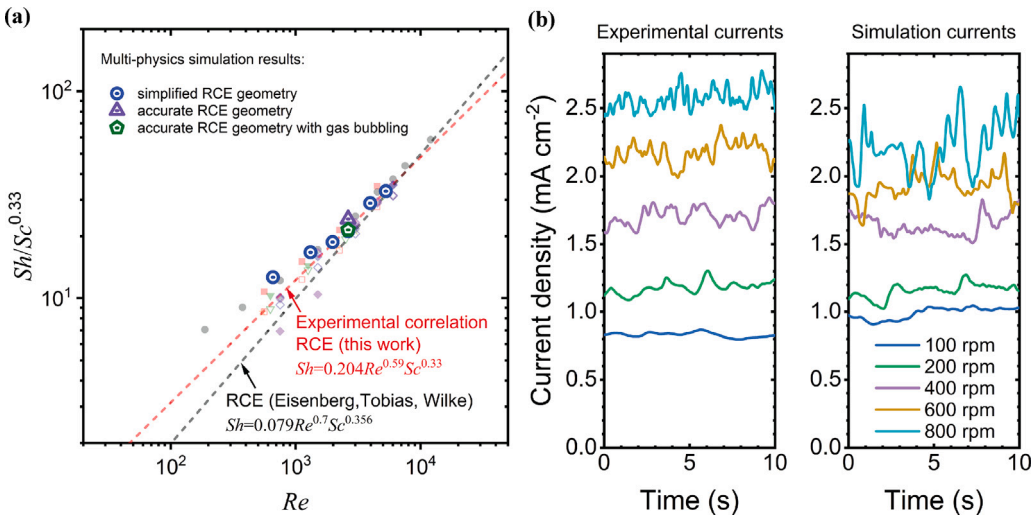

Fig. 6. Simulated currents for ferricyanide reduction and development of dimensionless relationships between transport and hydrodynamics for results obtained in the multi-physics model of the RCE reactor. (a) Relationship between Sherwood and Reynolds numbers extracted from the multi-physics models and their comparison to experimental relations extracted for the RCE reactor. Experimental data from Fig. 2(b) is shown in the background for comparison. Detailed experimental methods are reported in [7]. (b) Comparison of transient behavior of the RCE current density for ferricyanide reduction at different rotation speeds under mass transport limited conditions, showing the fluctuations caused by vortices near the surface. A 0.1 M potassium perchlorate solution with the addition of 0.01 M potassium ferricyanide was used as electrolyte for the ferricyanide reduction experiments.

surprising, as the diffusion boundary layer is significantly smaller than the viscous sub-layer due to the large *Sc* number used in this study.

Further comparison can be made between the effects of the two geometries by examining the flow patterns of the fluid presented in Fig. 7. Here, Fig. 7(a) and (b) show a vertical and horizontal cross-section of the fluid flow patterns in the simplified geometry, while Fig. 7(c) and (d) show the same cross-sections for the accurate geometry. All images are taken at steady-state flow conditions for a cylinder rotation speed of 400 rpm. The horizontal cross-sections are taken at the center of the catalyst, as shown by the red dashed line. The color scale tied to the fluid velocity delineates two main regions in the liquid phase of the reactor. Near the rotating shaft, steep velocity gradients occur where surface vortices can be differentiated. Fluid velocity quickly decreases with increasing distance from the surface, and a relatively low velocity region can be observed in the bulk of the fluid shown in blue. Here, large vortices can be identified in this bulk region spanning the annular space between the shaft and the outer wall of the reactor. Slight differences in the flow of bulk fluid can be identified between the two geometries caused by the reference electrode, gas sparger, and counter electrode channel. However, the region close to the electrode that is relevant to electrocatalysis appears identical between the two geometries. In evaluating the effect of bulk flow patterns on mass transport at the surface, a simple comparison can be made between the velocity field shown in the bulk and near the shaft surface. The color scale indicates that fluid near the shaft surface is an order of magnitude higher for velocity relative to the fluid in the bulk. This alone is enough to suggest that disruptions in the bulk of the fluid are unlikely to contribute significantly to the mechanisms of mass transport near the surface of the catalyst, and further validates the assumptions made in simplifying the geometry. This holds true, at least, under conditions of high electrode rotation speeds shown in Fig. 7.

5.1. Structured flow patterns in the RCE reactor

Now that simulation results have been shown to agree with our experimental observations, a detailed analysis of the simulation results can be used to gain insight about the mechanisms driving mass transport in the RCE. Under the reaction conditions investigated here, we find that two regions with structured vortex formation occur in the RCE reactor. Bulk vortices are identified spanning the annular space between the rotating shaft and the reactor walls, and surface vortices form inside the hydrodynamic boundary layer, close to the electrode surface. Beginning with the bulk vortices, one might be tempted to identify these as Taylor vortices. Taylor vortices have been well documented and are widely known to develop in fluid between rotating concentric cylinders [32–34]. CFD simulations of rotating cylinders consistently predict the formation of Taylor vortices as well: especially with generalized wall functions and coarse mesh [35–38]. This result is to be expected, since Taylor vortices are structured flow patterns that form outside the viscous sublayer and unstructured turbulent layer. However, as depicted in Fig. 7(a) and (c), only one large vortex is formed in the RCE. If stable Taylor vortices were to form, semi-uniform counter rotating vortex pairs would be expected with approximately equal width and height across the annular space. In fact, this behavior is observed in the first few seconds after rotation of the shaft is initiated, which is also visualized in Video 1 (Supplementary data in Appendix A).

As the simulation time progressed, the Taylor vortices were quickly disrupted by the formation of smaller vortices near the surface of the electrode and a significant edge effect caused by the base of the shaft. The role of the edge effect can be discerned in Video 1 of the Supplementary data, and in the still images in Fig. 7 where the fluid near the base of the reactor flows up near the electrode and down at the reactor wall. This edge effect is caused by the bottom of the shaft where the rotating surface pulls fluid from below to replace fluid being ejected from the sides by centrifugal force. At the outer wall of the reactor, fluid is being pulled down to replace fluid under the shaft, while the fluid around the base of the shaft is directed upward. The effect is most pronounced at low rpm where the azimuthal velocity of the fluid is lower, and is overshadowed by azimuthal fluid motion as rpm is increased, which is shown in Fig. 8(a) by the disappearance of the bulk vortex as rpm is increased. At first glance, the behavior of the vortex in the bulk might be confused with a Taylor vortex, but the originating mechanism is quite different.

The second distinct region of fluid presented in Fig. 7 is the region near the surface of the shaft where small, high intensity vortices form in counter rotating pairs. These vortices remain relatively stable on the surface, increase in frequency with rotation speed, and move across the surface as shown in Video 1 in the Supplementary data. Looking at Fig. 8(a) and (b), we see that these vortices also become more

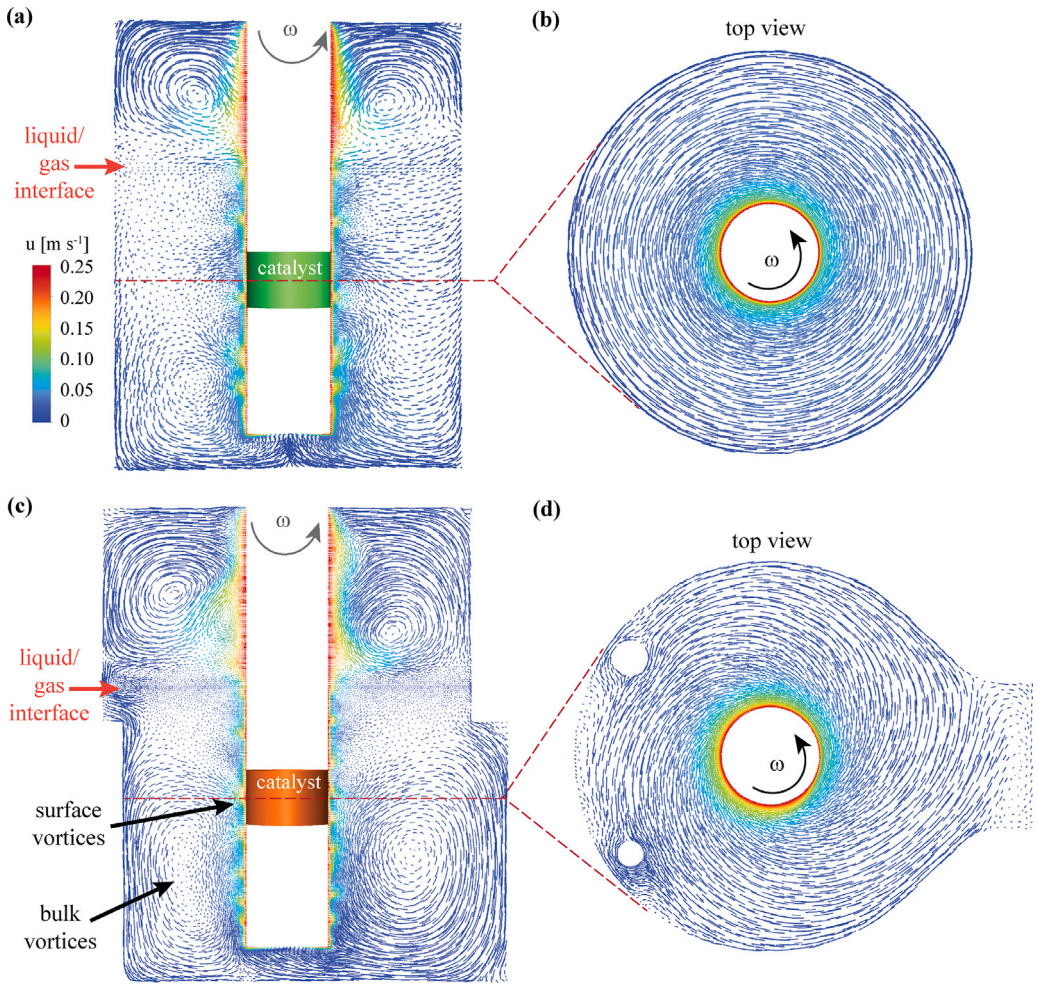

Fig. 7. Cross-sections of the (a,b) simplified and (c,d) accurate geometry showing the flow patterns of fluid in the RCE reactor at 400 rpm. (b) and (d) show horizontal cross-sections at the location indicated by the red dashed line. Fluid behavior is similar for both geometries, especially in the region close to the shaft surface that is most significant for electrochemical transformations. Here structured vortices cause local disruptions to mass transfer at the catalyst surface while bulk vortices have a negligible effect on the near wall region.

compact with increasing rotation speed, and appear to have a non-trivial influence on fluid motion close to the electrode surface. The size of these vortices appears to be tied to velocity gradient. In Fig. 8(b) we can see that as the gradient increases with rpm, represented by an increase in color gradient. These vortices also become smaller in Fig. 8(a) and move closer to the surface as illustrated in Fig. 8(b). Vortices particularly similar to these, named Görtler vortices, have previously been shown to occur inside the laminar sub-layer near curved surfaces where steep velocity gradients occur [39]: like those found in this RCE. These vortices are known to develop simultaneously with Taylor vortices and are thought to be a key mechanism in the transition from structured vortex formation to bulk, unstructured turbulent flow [40]. The formation of surface vortices , along with the flow pattern caused by the bottom surface of the shaft, is likely why Taylor vortices are not observed in this RCE at steady-state flow conditions.

5.2. Analysis of surface vortex effects

While azimuthal velocity is still dominant near the surface, we can see that the surface vortices do influence the fluid motion in the radial and axial directions. In between the vortex pairs, a jet-like feature forms where fluid is pulled away from the surface. This feature is best shown in Fig. 8(b) for 300 rpm. This jet-like feature is tied to a local expansion of the diffusion boundary layer caused by an increased resistance to diffusion in the direction of the catalyst resulting from the radial velocity influence in that region. This behavior is best shown in Fig. 8(c) for 100 and 300 rpm. At the outer edges of the vortex pairs, fluid is directed toward the shaft surface, while directly under the vortex, fluid is directed across the surface in the axial direction. This results in increased mass transfer by bringing bulk fluid close to the surface, and a reduction in the local diffusion boundary layer thickness. This effect is best shown in Fig. 8(c) for 200 and 400 rpm. It should be noted, that while the local diffusion boundary layer thickness is slightly changed by the presence of these vortices, the average value is still dominated by the random turbulence modeled by the $\kappa - \epsilon$ method. However, these local fluctuations in diffusion boundary layer thickness result in local variation in mass transfer rates to the catalyst surface, and are most likely the source of fluctuations in the current density that we observe in the simulations. These surface vortices can be thought of as an additional convective transport mechanism that is unique to the rotating cylinder geometry. The minor role that these vortices play in determining mass transfer rates can be examined by comparing the scale of the vortices to the scale of the diffusion boundary layer. In Fig. 8(d) we see that the hydrodynamics boundary layer calculated from the velocity gradient at the surface ranges between 400 and 1600 μm, while Fig. 8(e) shows that the diffusion boundary layer calculated from the concentration gradient at the surface ranges from 25 to 75 μm. By revisiting Fig. 8(a), (b), and (c) we can see which effects are influential at these different scales. Notably, in Fig. 8(b) and (c) we can see that the region of swirling fluid where surface vortices are present,

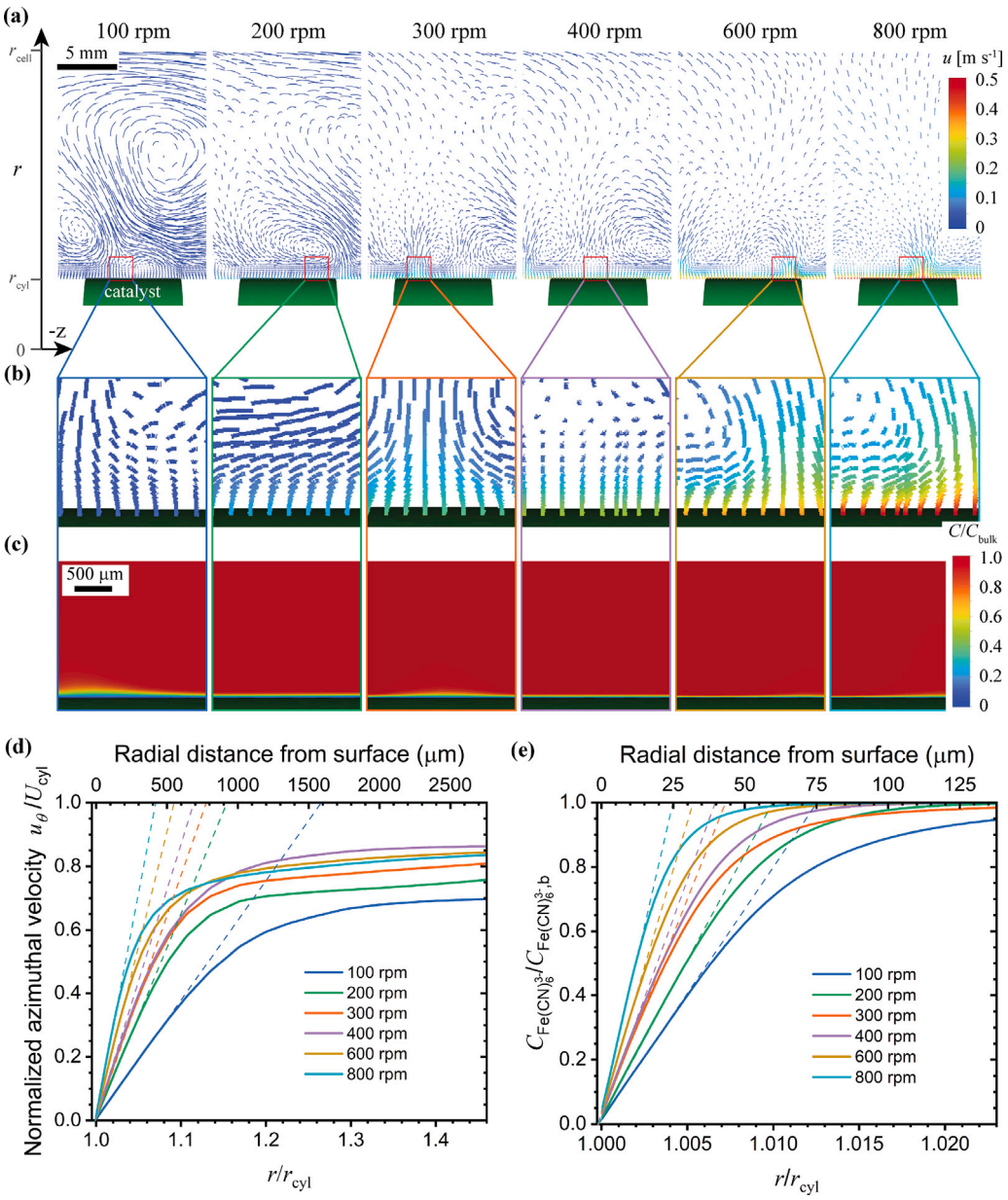

Fig. 8. (a) Cross sections of the fluid normal to the electrode surface showing fluid flow patterns at each rotation speed. (b) Close up of the fluid flow patterns at the electrode surface showing how the effects of the surface vortices move closer to the electrode surface as rotation speed is increased and how the velocity gradient increases. (c) Heat maps of ferricyanide concentration at different rpm showing the influence of the surface vortices on the diffusion boundary layer and how increasing rotation speed reduces the diffusion boundary layer thickness. Normalized boundary layers profiles for (d) azimuthal velocity and (e) ferricyanide concentration, showing the reduction in boundary layer size for each as a function of rpm.

is far from the region of fluid containing the diffusion boundary layer. Even at 800 rpm, where both boundary layers are the most compact, the velocity in the azimuthal direction (out of plane) is aligned with the surface, showing that the vortices have minimal influence in that region.

While the fluctuations caused by these surface vortices may at first appear to be problematic for the investigation of intrinsic kinetics, a few points should be noted. First, the variation of the local mass transfer rates is small in comparison to the magnitude of the total mass transfer rates. These mass transfer rates can be studied by comparing the amplitude of the current density fluctuations to the magnitude of the current density in Figs. 6(b), 1(c), 1(d), and 1(e). Second, these fluctuations are due to a convective mixing action that enables control of the mass transfer rate at the surface by controlling the rotation speed. The change in mass transfer rates due to increased convection is far greater than local fluctuations. This change can be examined by comparing the change in current density magnitude as the rotation speed is increased, to the amplitude of the fluctuation in Figs. 6(b), 1(c), 1(d), and 1(e). With the variation in local mass transfer rates being so small in comparison to other effects, the RCE should still allow for the effects of mass transport and intrinsic kinetics to be decoupled effectively.

Current density fluctuation observed in the simulated and experimental studies reported here, are common to many experimental electrochemical reactors that are used to study intrinsic kinetics. In comparison to these, the RCE offers the distinct advantage of being able to precisely define the mass transport conditions over a large catalyst surface whereas other reactors (especially those with large surface areas such as the compression H-cell commonly used in electrochemical CO_2 reduction studies) have poorly defined hydrodynamics conditions that can be significantly influenced by slight variations in experimental conditions, such as the rate at which gas is bubbled through the bulk

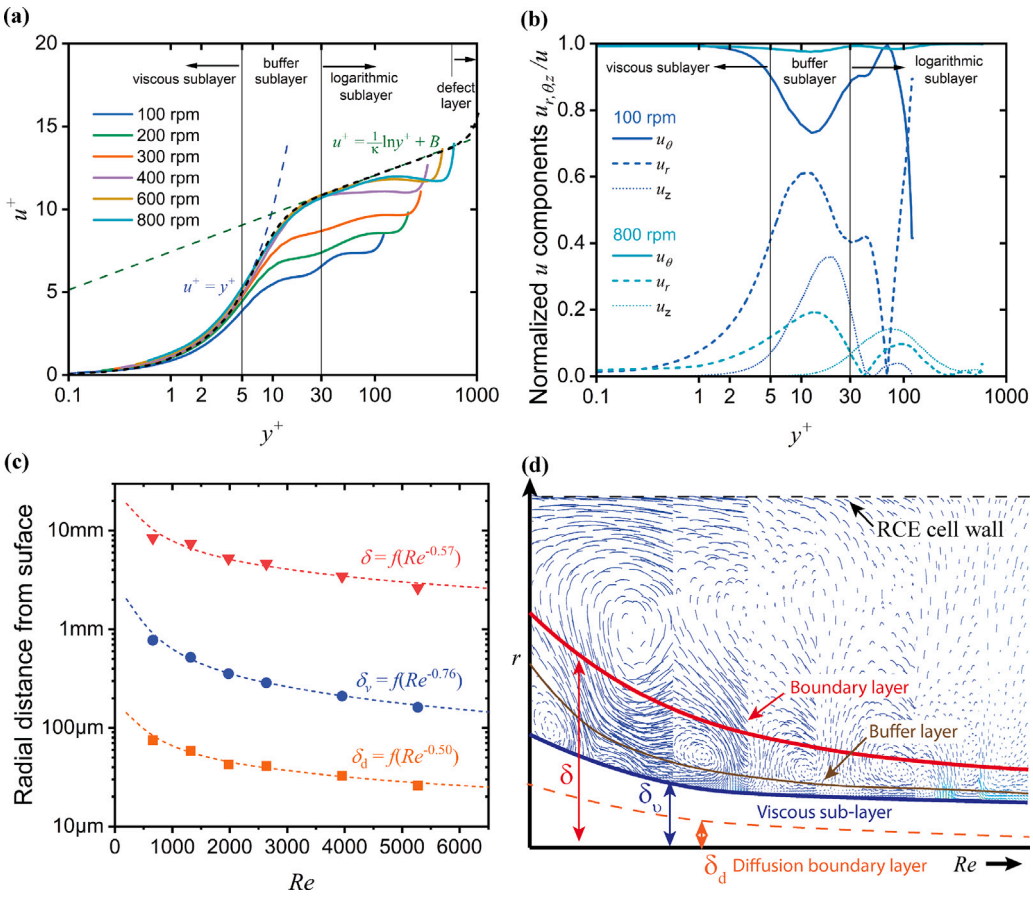

Fig. 9. (a) Nondimensionalized velocity (u^+) vs. distance from the wall (y^+) showing the degree of agreement between simulated velocity profiles and experimentally measured, universal velocity profiles for turbulent flow over a smooth surface. Here κ is the Von Kármán constant, 0.41, and B is experimentally determined to be 5 for turbulent flow. Profiles at low rpm deviate significantly from ideal behavior due to vortex contributions. (b) Relative contributions of each component of the total velocity vector vs. y^+. Here, the velocity component is normalized to the magnitude of the total velocity to show how at low rotation speeds, radial and velocity components contribute more significantly than at high rpm. (c) Hydrodynamic boundary layer (δ when u is 99% of the bulk velocity), viscous sublayer (δ_v), and diffusion boundary layer (δ_d) thicknesses and their dependence on Re. (d) Exaggerated representation of the different boundary layer regions showing their positions relative to each other and how they change with Re. The background shows how the flow field develops so that surface vortices are contained in the region between δ and δ_v and bulk flow vortices are overcome by the azimuthal velocity.

of the solution or the rate of rotation of the stirrers reported to be used in some of these cells.

5.3. Effects of rotation speed on boundary layer development

Further insight as to the behavior and contribution of both the bulk and surface vortices can be gained by comparing the nondimensionalized hydrodynamics boundary layer profiles. Fig. 9(a) shows the nondimensional velocity (u^+) vs. the nondimensional distance (y^+) for each rotation speed averaged at three lines located at 1/4, 1/2, and 3/4 of the electrode height. These are compared to the universal boundary layer profile for turbulent flow over a smooth surface, indicated by the dashed lines. Inside the laminar sublayer $u^+ = y^+$, while in the turbulent or logarithmic sublayer u^+ is a logarithmic function of y^+. Between these two layers, the velocity holds to a blended function of the two regions. In the logarithmic relationship, κ is the Von Kármán constant 0.41, and B has been experimentally determined to be 5 for turbulent flow over a smooth surface. In our simulations, we see that at low rotation speeds of 100 to 300 rpm, the profile deviates significantly from the universal profile, while at speeds above 400 rpm, the profiles behave more ideally. This correlates with what we see in Fig. 6(a) where at low Re, Sh is higher than the correlation would suggest it should be. The reason for this deviation from ideal behavior can be identified by comparing the relative contributions of each component in the velocity vectors depicted in Fig. 9(b). Here, the magnitude of each velocity component is divided by the magnitude of the total velocity vector to show the contribution of each component relative to the total velocity magnitude. 100 and 800 rpm are compared to provide contrast between low and high rotation speeds. At both 100 and 800 rpm, u_θ is the dominant component of the velocity across most of the fluid. However, at low rpm, u_r and u_z contribute far more significantly than at high rpm. Notable contributions from u_r can be observed as close to the surface as $y^+ = 2$ (well inside the viscous sublayer). At high rpm similar levels are not reached until $y^+ = 10$ (in the buffer layer). Under vortex free flow, there would be little to no u_r or u_z contributions.

These contributions from u_r and u_z originate from the development of vortices that mix fluid near the wall with fluid from the bulk. The mixing action of these vortices causes two significant effects. First, low and high velocity fluid are mixed in regions where vortices are influential. This behavior is why the velocity (u^+) is lower in the regions where u_r and u_z have significant contributions. At higher rpm, this vortex induced mixing action is less influential than the momentum being transferred from the wall and the velocity increases until it aligns with the universal velocity profile as illustrated in Fig. 9(a). There, the direction of fluid flow is primarily aligned with the rotation of the shaft in the azimuthal direction. The second effect is that this vortex induced mixing action also enhances mass transport of reactants by bringing bulk concentration fluid to the surface and mixing it with lower concentration fluid in the boundary layer. This effect is why the Sh is higher than the expected value for 100 and 200 rpm. Here the influence of the surface vortices is simply significant enough in regions near the diffusion boundary layer to enhance mass transport. It is

especially helpful to note, that the outer edge of the diffusion boundary layer is located at $y^+ = 1$ for all rotation speeds. Knowing this result, we can again refer to Fig. 9(b) and see that at 100 rpm, u_r does indeed influence regions closer to the surface than $y^+ = 1$, suggesting that vortices do influence the concentration boundary layer at these lower rotation speeds. In contrast, at the highest rotations speeds such as 800 rpm, u_r does not start becoming influential until $y^+ > 1$. Explained simply, at low rotation speeds, the increased contributions of u_r and u_z signify an increased convective mass transport effect caused by vortex formation that is reduced as rpm is increased and both δ_v and δ_d are compressed closer to the wall.

Finally, the extraction of boundary layer thicknesses enables the identification of their relationship to rotation speed and to each other. Three boundary layers of importance are plot as a function of *Re* in Fig. 9(c). The hydrodynamic boundary layer, δ is found to relate to the *Re* by an exponent of −0.57. Here δ is defined as the distance from the wall where 99% of the bulk velocity is reached. We can see that as *Re* is increased, δ decreases from around 10 mm at 100 rpm, to 2 mm at 800 rpm. As shown in the exaggerated representation of the flow development observed in Fig. 9(d), the surface vortices fall inside this boundary layer.

The viscous sublayer, δ_v on the other hand, falls in the 0.1 to 1.0 mm range: below the region where surface vortices form. Here δ_v is defined as the distance from the surface at $y^+ = 5$. In this region, azimuthal velocity dominates and nearly laminar flow is observed as shown in Fig. 9(a) and (b). We find that δ_v is related to *Re* by a power of −0.76 shown in Fig. 9(c). Since y^+ is normalized by the shear stress at the wall, and the shear stress is proportional to the velocity gradient at the wall, this means that the velocity gradient at the wall has an identical dependency on *Re*. For flow over a flat plate, the laminar boundary layer was found by the Blasius solution to have a power of −0.5 dependency on *Re*. Thus, we find that the effect of turbulence on the laminar sublayer is the difference in exponent of −0.26, indicating that the laminar sublayer is smaller than what would be expected for laminar flow.

Likewise, the diffusion boundary layer is plotted as δ_d where we see a dependency on *Re* to the power of −0.5. In this case, δ_d is defined as the linear diffusion boundary layer thickness calculated by the concentration gradient at the wall and the bulk concentration of ferricyanide. δ_d is observed to be in the range of tens of micrometers and is deep inside the viscous sublayer. It should be noted here that δ_d is the linear approximation presented in Fig. 8(e) and does not capture the enhanced mass transfer caused by convection at the outer edge of the diffusion boundary layer. This relationship of $Re^{-0.5}$ is significant in that the same relationship is observed for Fickian diffusion in the RDE described by the Levich equation [14]. This result tells us that at a region near the wall of the electrode, mass transport is described by Fickian diffusion. It must be noted here that Fickian diffusion can be applied only for simple electrocatalytic transformations, such as the reduction of ferricyanide, as this electrocatalytic process does not involve the reabsorption and further transformation of reaction intermediates. As pointed out in Section 3, Fickian diffusion cannot be applied to rationalize stochastic transport-reaction processes relevant to more complex electrocatalytic processes, such as the reduction of CO_2 on copper electrodes. Additionally, we know that δ_d is inversely proportional to *Sh* which means that mass transport in our reactor is related to the *Re* in our RCE reactor as expressed in Eq. (7) by a power of −0.59. From this relationship, we can then determine that the turbulent contribution to mass transport at the catalyst surface is described by the difference in the exponent experimentally measured and that calculated for the local mass transfer within the first layers of fluid at the electrode (−0.09). Lastly, from literature, it is commonly known that the diffusion boundary layer thickness is proportional to the laminar boundary layer thickness by $Sc^{-1/3}$ for flow over a flat plate. However, using the relationships we have determined here, we see that there is an additional dependency of the Reynolds to the power of 0.26 such that $\delta_d \propto \delta_v Re^{0.26} Sc^{-1/3}$. Note that while changing the properties of the dilute reacting species in the solution will change δ_d, the effects of the hydrodynamic boundary layer behavior will remain the same.

The effect of the electrode roughness on the hydrodynamics around the RCE has not been discussed here, but it is also an important parameter for electrocatalysis. As the viscous sublayer thickness in the rotations studied here remains large and in the order of a few tens of micrometers, the RCE cell should allow the decoupling of internal and external mass transport in porous electrodes where the length of the pore is smaller than the viscous sublayer, which is the case for most of the nanostructured coatings used in catalysis where the porous catalyst films range from a few nanometers to a few micrometers in size. Depending on the roughness and aspect ratio of the porous film, however, it is expected that roughness will start to play a role in affecting the structure of the viscous sublayer as the dimensions of the catalyst particles and the viscous sublayer thickness become closer in magnitude.

6. Conclusions

Developing advanced electrochemical reactors capable of efficiently producing chemicals at industrial scales requires a deep understanding of the underlying processes that govern reactor performance. The complex interactions between mass, energy, and charge transport as well as reaction kinetics makes acquiring this understanding difficult, especially when attempting to apply these principles across multiple scales. Developing reliable relationships requires collection of high fidelity data sets with specialized reactors, like the gastight RCE, that enable the contributions of individual effects to be decoupled. Still, effectively utilizing the information gained by these experiments to inform the design of large scale reactors can be difficult due to the nonlinear complexity of the mass, heat, and charge phenomena involved. Utilization of multiscale computer modeling can enable the combination of these effects into a single model that covers a wide range of time and length scales. With correctly defined parameters, multiscale modeling methods such as CFD, MD, and DFT can be integrated to provide accurate simulations of complex reactor behavior and provide detailed information about the intrinsic behavior of a reactor. This information can then be used to inform the design of industrial scale reactors or even test these designs *in silico*.

Here we have provided a detailed account of the first step in our development of a CFD model capable of capturing the performance of our gastight RCE reactor. In the pursuit of a model that can predict the behavior of our reactor for CO_2 reduction, we have divided the model development into a series of experimentally verifiable stages. The first stage, presented here, is establishing the hydrodynamics in the reactor. This was accomplished by developing a simplified model capable of simulating the transient and time averaged behavior of the mass transport limited ferricyanide reduction reaction. Under the conditions of interest in this reactor, the diffusion boundary layer is well within the hydrodynamic boundary layer. Turbulent flow is known to disrupt this diffusion boundary layer, causing frequent low intensity fluctuations in the current density that can be detected experimentally. Capturing this unique behavior was the key to ensure an accurate model of the hydrodynamics in revealing the need to utilize enhanced surface treatments and fine mesh to describe the electrode/electrolyte interface.

We find that surface vortex formation near the outer edge of the viscous sub-layer is primarily responsible for these fluctuations. The ability of the model to capture this behavior as well as the correct magnitude of the current density across a rotation speed range of 100–800 rpm is primarily due to two features of the simulation: the use of an enhanced surface treatment method and a fine mesh near the surface. Due to the small size of the diffusion boundary layer compared to the hydrodynamic boundary layer, an appropriately fine mesh was required near the electrode surface to capture the concentration gradient. On

the other hand, the enhanced surface treatment method implemented a two-layer approach to model fluid flow near the wall that allowed for the use of this fine mesh near the surface, and a coarse mesh in the bulk of the fluid. This refined mesh near the surface was also responsible for allowing the model to capture the development of surface vortices in the near wall region. We also note that this characteristic flow pattern can be obscured by a more coarse mesh and simplified wall treatment. Additional simulations with a reactor accurate geometry also show that changes in the bulk flow outside the boundary layer, have minimal effect on the performance of the reactor model, which is consistent with experimental observations. We find that as the rotation speed increases and the boundary layer shrinks, the effect of the surface vortices is shown by an increase in amplitude and frequency of current density fluctuations. However, above 400 rpm the change in boundary layer thickness is smaller relative to the change in rpm and the frequency of surface vortices increases, thus causing a reduction in amplitude and an increase in frequency of current density fluctuation.

In addition to capturing the transient behavior of the RCE reactor, the simulation also captures the relationship between *Sh* and *Re* that was previously determined for this RCE reactor and closely aligns with other published correlations. The simulation method presented here was found to provide an accurate representation of the hydrodynamics of the RCE that are pertinent to modeling electrochemical reactions at the surface of the electrode. This method can be applied to reactors with similar architecture to provide insight into the hydrodynamics of the reactor. Future work will systematically add electrochemical reactions to the RCE CFD model in a way that allows for each simulation improvement to be experimentally verified until a model is created that can accurately predict the performance of CO_2 reduction in the RCE.

CRediT authorship contribution statement

Derek Richard: Conceptualization, Data curation, Formal analysis, Investigation, Methodology, Software, Validation, Visualization, Writing – original draft, Writing – review & editing. **Matthew Tom:** Conceptualization, Data curation, Formal analysis, Investigation, Methodology, Software, Validation, Visualization, Writing – original draft, Writing – review & editing. **Joonbaek Jang:** Conceptualization, Data curation, Formal analysis, Investigation, Methodology, Writing – original draft, Writing – review & editing. **Sungil Yun:** Conceptualization, Data curation, Formal analysis, Investigation, Methodology, Software, Writing – original draft, Writing – review & editing. **Panagiotis D. Christofides:** Conceptualization, Data curation, Formal analysis, Funding acquisition, Investigation, Methodology, Software, Project administration, Resources, Supervision, Validation, Visualization, Writing – original draft, Writing – review & editing, Conceived the idea, Supervision. **Carlos G. Morales-Guio:** Conceptualization, Data curation, Formal analysis, Funding acquisition, Investigation, Methodology, Software, Project administration, Resources, Supervision, Validation, Visualization, Writing – original draft, Writing – review & editing, Conceived the idea, Supervision.

Declaration of competing interest

The authors declare the following financial interests/personal relationships which may be considered as potential competing interests: Carlos G. Morales-Guio reports financial support was provided by Office of Energy Efficiency and Renewable Energy.

Data availability

Data will be made available on request.

Acknowledgments

We would like to gratefully acknowledge financial support from the U. S. Department of Energy, through the Office of Energy Efficiency and Renewable Energy (EERE), under the Advanced Manufacturing Office Award Number DE-EE0007613.

Appendix A. Supplementary data

Supplementary material related to this article can be found online at https://doi.org/10.1016/j.electacta.2022.141698.

References

[1] Fossil Fuel Energy Consumption (% of Total), The World Bank, 2014, https://data.worldbank.org/indicator/EG.USE.COMM.FO.ZS.
[2] P.D. Luna, C. Hahn, D. Higgins, S.A. Jaffer, T.F. Jaramillo, E.H. Sargent, What would it take for renewably powered electrosynthesis to displace petrochemical processes? Science 364 (6438) (2019) eaav3506.
[3] J. Newman, N.P. Balsara, Electrochemical Systems, John Wiley & Sons, 2021.
[4] F. Walsh, G. Kear, A. Nahlé, J. Wharton, L. Arenas, The rotating cylinder electrode for studies of corrosion engineering and protection of metals—An illustrated review, Corros. Sci. 123 (2017) 1–20.
[5] C.J. Low, C.P. de Leon, F.C. Walsh, The rotating cylinder electrode (RCE) and its application to the electrodeposition of metals, Aust. J. Chem. 58 (4) (2005) 246–262.
[6] J. Newman, Current distribution on a rotating disk below the limiting current, J. Electrochem. Soc. 113 (12) (1966) 1235.
[7] J. Jang, M. Rüscher, M. Winzely, C.G. Morales-Guio, Gastight rotating cylinder electrode: Toward decoupling mass transport and intrinsic kinetics in electrocatalysis, AIChE J. 68 (5) (2022) e17605.
[8] D. Clark, H. Malerød-Fjeld, M. Budd, I. Yuste-Tirados, D. Beeaff, S. Aamodt, K. Nguyen, L. Ansaloni, T. Peters, P.K. Vestre, D.K. Pappas, M.I. Valls, S. Remiro-Buenamañana, T. Norby, T.S. Bjørheim, J.M. Serra, C. Kjølseth, Single-step hydrogen production from NH_3, CH_4, and biogas in stacked proton ceramic reactors, Science 376 (6591) (2022) 390–393.
[9] T. Mizushina, The electrochemical method in transport phenomena, in: T.F. Irvine, J.P. Hartnett (Eds.), Adv. Heat Transfer 7 (1971) 87–161.
[10] J.R. Selman, C.W. Tobias, Mass-transfer measurements by the limiting-current technique, in: T.B. Drew, G.R. Cokelet, J.W. Hoopes, T. Vermeulen (Eds.), Adv. Chem. Eng. 10 (1978) 211–318.
[11] M. Eisenberg, C.W. Tobias, C.R. Wilke, Ionic mass transfer and concentration polarization at rotating electrodes, J. Electrochem. Soc. 101 (6) (1954) 306–320.
[12] D.C. Silverman, The rotating cylinder electrode for examining velocity-sensitive corrosion—A review, Corrosion 60 (11) (2004) 1003–1023.
[13] J. Selman, J. McClure, Limiting current to a vertical rotating rod electrode, J. Electroanal. Chem. Interfacial Electrochem. 110 (1) (1980) 79–92.
[14] V.G. Levich, Physicochemical Hydrodynamics, Prentice-Hall Inc., 1962.
[15] K.P. Griffin, L. Fu, P. Moin, Velocity transformation for compressible wall-bounded turbulent flows with and without heat transfer, Proc. Natl. Acad. Sci. 118 (34) (2021) e2111144118.
[16] S. Vijay, W. Ju, S. Brückner, S.-C. Tsang, P. Strasser, K. Chan, Unified mechanistic understanding of CO_2 reduction to CO on transition metal and single atom catalysts, Nature Catal. 4 (12) (2021) 1024–1031.
[17] D. Micale, C. Ferroni, R. Uglietti, M. Bracconi, M. Maestri, Computational fluid dynamics of reacting flows at surfaces: Methodologies and applications, Chem. Ing. Tech. 94 (5) (2022) 634–651.
[18] G. Bauer, P. Gamnitzer, V. Gravemeier, W.A. Wall, An isogeometric variational multiscale method for large-eddy simulation of coupled multi-ion transport in turbulent flow, J. Comput. Phys. 251 (2013) 194–208.
[19] P. Van Shaw, T.J. Hanratty, Fluctuations in the local rate of turbulent mass transfer to a pipe wall, AIChE J. 10 (4) (1964) 475–482.
[20] D. Matić, B. Lovreček, D. Skansi, The rotating cylinder electrode, J. Appl. Electrochem. 8 (5) (1978) 391–398.
[21] ANSYS, Ansys Fluent Theory Guide, ANSYS Inc., Canonsburg, PA, 2022.
[22] B.E. Launder, N.D. Sandham, Closure Strategies for Turbulent and Transitional Flows, Cambridge University Press, 2002.
[23] T.-H. Shih, W.W. Liou, A. Shabbir, Z. Yang, J. Zhu, A new $k-\epsilon$ eddy viscosity model for high Reynolds number turbulent flows, Comput. & Fluids 24 (3) (1995) 227–238.
[24] M. Wolfshtein, The velocity and temperature distribution in one-dimensional flow with turbulence augmentation and pressure gradient, Int. J. Heat Mass Transfer 12 (3) (1969) 301–318.
[25] H.C. Chen, V.C. Patel, Near-wall turbulence models for complex flows including separation, AIAA J. 26 (6) (1988) 641–648.
[26] T. Jongen, Y. Marx, Design of an unconditionally stable, positive scheme for the $K-\epsilon$ and two-layer turbulence models, Comput. & Fluids 26 (5) (1997) 469–487.

[27] F. White, G. Christoph, A Simple New Analysis of Compressible Turbulent Two-Dimensional Skin Friction Under Arbitrary Conditions, Technical Report, University of Rhode Island, Kingston, Department of Mechanical Engineering and Applied Mechanics, 1971.
[28] P.G. Huang, P. Bradshaw, T.J. Coakley, Skin friction and velocity profile family for compressible turbulent boundary layers, AIAA J. 31 (9) (1993) 1600–1604.
[29] B. Kader, Temperature and concentration profiles in fully turbulent boundary layers, Int. J. Heat Mass Transfer 24 (9) (1981) 1541–1544.
[30] W. Haynes, CRC Handbook of Chemistry and Physics, CRC Press, 2016.
[31] M. Eisenberg, C. Tobias, C. Wilke, Mass Transfer in Electrode Processes. 2. Mass Transfer at Rotating Cylinders, Technical Report, University of California, Berkeley, Department of Chemistry and Chemical Engineering, 1953.
[32] D.R. Gabe, G. Wilcox, J. Gonzalez-Garcia, F. Walsh, The rotating cylinder electrode: its continued development and application, J. Appl. Electrochem. 28 (8) (1998) 759–780.
[33] C.D. Andereck, S.S. Liu, H.L. Swinney, Flow regimes in a circular couette system with independently rotating cylinders, J. Fluid Mech. 164 (1986) 155–183.
[34] M. Sprague, P. Weidman, S. Macumber, P. Fischer, Tailored Taylor vortices, Phys. Fluids 20 (1) (2008) 014102.
[35] E. Rivero, P. Granados, F. Rivera, M. Cruz, I. González, Mass transfer modeling and simulation at a rotating cylinder electrode (RCE) reactor under turbulent flow for copper recovery, Chem. Eng. Sci. 65 (10) (2010) 3042–3049.
[36] R. Srinivasan, S. Jayanti, A. Kannan, Effect of Taylor vortices on mass transfer from a rotating cylinder, AIChE J. 51 (11) (2005) 2885–2898.
[37] F.J. Almazán-Ruiz, F.V. Caballero, M.R. Cruz-Díaz, E.P. Rivero, I. González, Scale-up of rotating cylinder electrode electrochemical reactor for Cu(II) recovery: Experimental and simulation study in turbulence regimen, Electrochim. Acta 77 (2012) 262–271.
[38] T. Perez, J. Nava, Simulation of turbulent flow of a rotating cylinder electrode. influence of using plates and concentric cylinder as counter electrodes, Int. J. Electrochem. Sci. 8 (2013) 4690–4699.
[39] W.S. Saric, Görtler vortices, Annu. Rev. Fluid Mech. 26 (1) (1994) 379–409.
[40] T. Wei, E.M. Kline, S.H.-K. Lee, S. Woodruff, Görtler vortex formation at the inner cylinder in Taylor–Couette flow, J. Fluid Mech. 245 (1992) 47–68.